Implementation and Optimization of Dosimetry for Theranostics in Radiopeptide Therapies

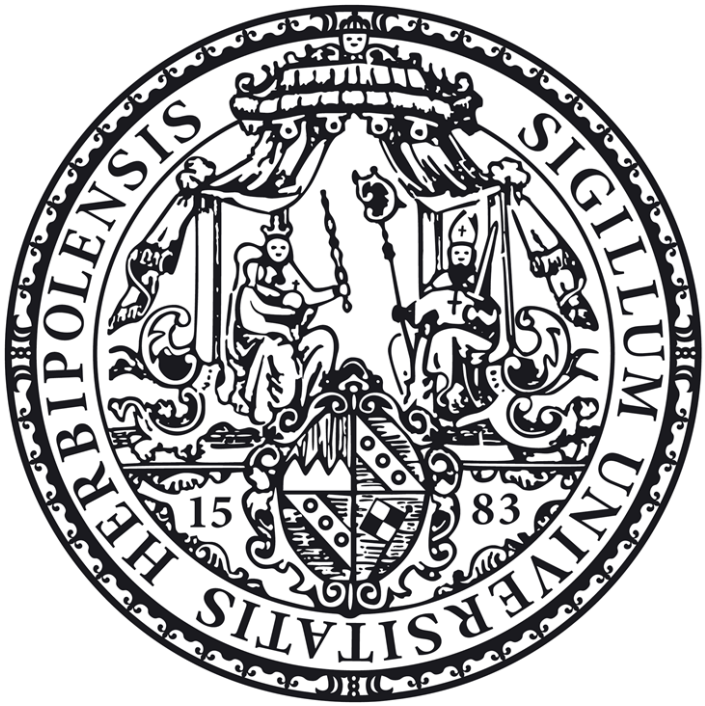

Doctoral thesis for a doctoral degree
at the Graduate School of Life Sciences,
Julius-Maximilians-Universität Würzburg,
Biomedicine, 2019

submitted by

Seval Beykan

from

Güzelyurt, Turkish Republic of Northern Cyprus

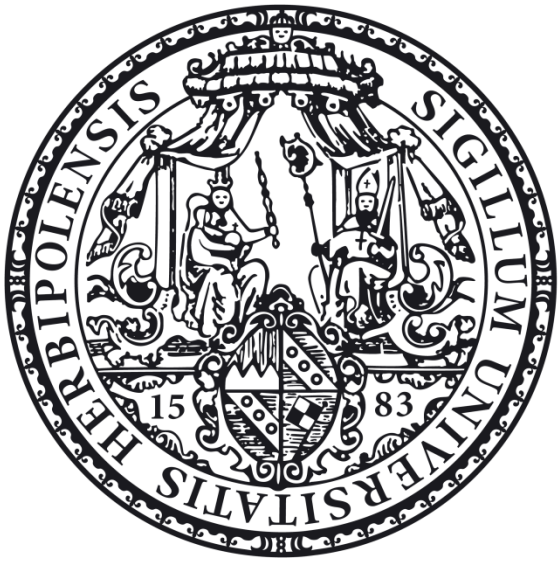

Implementation and Optimization of Dosimetry for Theranostics in Radiopeptide Therapies

Implementierung und Optimierung der Dosimetrie für die Theranostik in Radiopeptidtherapien

Doctoral thesis for a doctoral degree
at the Graduate School of Life Sciences,
Julius-Maximilians-Universität Würzburg,
Section Biomedicine

Submitted by

Seval Beykan

from

Güzelyurt, Turkish Republic of Northern Cyprus

Würzburg, 2019

Members of the Promotionskomitee:

Chairperson: Prof. Dr. med. Manfred Gessler

Primary Supervisor: Prof. Dr. Michael Lassmann

Supervisor (Second): Prof. Dr. Gerhard Glatting

Supervisor (Third): Prof. Dr. med. Andreas K. Buck

Date of Public Defence: ……

Date of Receipt of Certificates: ……

Submitted on: ……..……..

Office stamp

Table of Contents

i. Summary 8

i. Zusammenfassung 12

1. Introduction 16

2. Background 20

2.1. Radiation 20

2.2. Characteristic X-rays 20

2.3. Radioactive Decay 21

2.4. Emission Computed Tomography 23

2.5. SPECT/CT Imaging Technique 23

2.5.1. Acquisition 23

2.5.2. Reconstruction 24

2.5.3. Resolution and Partial Volume Effect 25

2.6. Somatostatin Receptors and Somatostatin Receptor Analogs 26

2.7. Radionuclides Used for Imaging and Therapy in Clinic 28

2.7.1. Properties of ^{68}Ga 29

2.7.2. Properties of ^{177}Lu 29

2.8. Peptide Receptor Radionuclide Therapy (PRRT) for NET 30

2.9. OPS201/202 Labelled Therapeutic and Diagnostic Radiopharmaceuticals 31

2.9.1. ^{177}Lu Labelled OPS201 Peptide for Therapy 31

2.9.2. ^{68}Ga Labelled OPS202 for Diagnostic Imaging 32

2.10. Dosimetry in Nuclear Medicine 33

2.10.1. General Concept of Dosimetry in Nuclear Medicine 33

2.10.2. Influence of the Reconstruction Parameters on Image Quantification with SPECT/CT 34

2.10.3. SPECT/CT Attenuation and Scatter Correction, Energy Window and Collimator Choice 35

2.10.4. Calibration Factor (System Sensitivity) Calculation 36

2.10.5. Activity Determination 37

2.10.6. Biokinetics and Biodistribution Assessment (Sampling Time Points and Frequency) 40

2.10.7. Time-Integrated activity Coefficient (TIAC) 40

2.10.8. Absorbed Dose and Effective Dose Calculation 41
3. Materials and Methods 44
3.1. Investigated Data and Analysis 44
3.2. Imaging with OPS202 and OPS201 in Each Species 45
3.3. In-vivo biodistribution and biokinetics analyses with OPS202 and OPS201 46
3.4. TIAC Calculation in each ^{177}Lu-OPS201, ^{68}Ga-OPS202 Injected Species 47
3.5. Blood and LV2-4 based Bone Marrow Dosimetry 48
3.6. Using IDAC-Dose2.1 and NUKDOS for Voxel Based Dosimetry 49
3.7. Scaling In Preclinical Studies for Estimating Human Dosimetry 50
3.8. 3D Printed Phantom Experiment 52
3.8.1 Preparation of 3D printed Phantom 52
3.8.2 Experimental Scans 53
4. Results 56
4.1. Dosimetry in Patients with OPS202 Used for Diagnostic Purposes 56
4.2. Dosimetry in Each Species with OPS201 Used for Therapeutic Purposes 60
4.3. Results Based on the Measurements of the 3D Printed Kidney Phantom 65
5. Discussion 68
6. Conclusion 72
7. List of Abbreviations 74
8. References 78
iii. Appendix 84
iv. List of Tables 90
v. List of Figures 92
vi. Affidavit / Eidesstattliche Erklärung 94
vii. Acknowledgments 96
viii. Curriculum Vitae 100

i. Summary

Peptide receptor radionuclide therapy (PRRT) is a molecular targeted radiation therapy involving the systemic administration of radiolabeled somatostatin receptor binding peptides designed to target with high affinity and specificity receptors overexpressed on tumors. Peptides are applied which either target as agonist (with internalization) or antagonist (little to no internalization). Recently, two novel antagonistic agents have been developed for clinical use: OPS202 and OPS201. ^{68}Ga-labelled OPS202 is used for diagnostic purposes with positron emission tomography and ^{177}Lu-labelled OPS201 is used for the therapy in patients with neuroendocrine tumors (NETs). Both agents are presently under clinical evaluation. Despite the very low internalization rate, the use of somatostatin receptor antagonists which target more binding sites on receptors are expected to result in higher specificity, more favorable pharmacokinetics and higher tumor retention and better visualization than the agonists.

The main goal of this thesis was analyzing the biodistribution, biokinetics and internal dosimetry of the recently developed somatostatin receptor antagonists (OPS201 and OPS202) for therapeutic and diagnostic purposes in different species (mice, pigs and patients). In addition, an analysis of the influence of image quantification and the integration of time activity curves on kidney dosimetry in a pig model was carried out. Furthermore, extrapolation methods, which are used for predicting organ absorbed doses for humans based on preclinical animal models, were systematically compared for blood, liver, and kidneys of OPS201 injected species.

Based on the OPS202 injected patients' investigations, ^{68}Ga-OPS202 shows promising biodistribution and imaging properties with tumor contrast which is optimal one hour after injection of the radiotracer. OPS202 is well tolerated and delivers absorbed doses to organs that are lower than those by ^{18}F-FDG and similar to other ^{68}Ga-labeled somatostatin receptor ligands. As a result of ^{68}Ga-OPS202 injection, the highest absorbed doses were observed in the urinary bladder (0.10 mGy/MBq) and kidneys (0.84 mGy/MBq). The calculated mean effective dose coefficient of ^{68}Ga-OPS202 injected patients was 0.024 mSv/MBq (3.6 mSv for 150 MBq ^{68}Ga-OPS202 injection) which is similar to other ^{68}Ga-labeled compounds.

Based on the OPS201 biokinetics and dosimetry investigations, after the injection of ^{177}Lu-OPS201, a fast blood clearance of the compound is observed in the first phase (half-life: 1.83 h) for each species. 10 min after injection, less than 5% of the injected activity per milliliter of blood circulates in pigs and humans. The analysis of the mice, pig and preliminary patient data provides evidence that, patients enrolled in a phase 1 ^{177}Lu-OPS201 trial would not be at risk of overexposure.

Based on our results, for ^{177}Lu labelled studies, late time points after 72 h have a great impact on absorbed dose calculations. That is why follow-up times especially at late time points (more than 72 h) are required for the time-integrated activity coefficient (TIAC) calculations in order to represent the area under the curve appropriately and to analyze both biokinetics and dosimetry accurately. In addition, to find the most adequate extrapolation methods that minimize the interspecies differences of dosimetry data, several extrapolation methods from animal to human have been tested. For OPS201 time scaling or combination of relative mass and time scaling results in most similar TIAC values, if the organ mass ratios between the species are high. In time scaling, the scan/sampling time is scaled by using the ratio of the whole body masses of the respective species. In relative mass scaling, the TIACs are scaled based on the ratio of the whole body and organ mass of respective species. Other methods tested showed higher deviations.

For the study on the influence of image quantification and the choice of the optimal scanning time points, a study in a pig model, which was performed in collaboration with Aalborg University and Octreopharm Sciences GmbH, was reanalyzed. As kidneys are organs-at-risk in PRRT with ^{177}Lu-labelled peptides, several quantification methods, based on 2D and 3D quantitative imaging were chosen. For this purpose, a 3D printed pig kidney phantom was prepared and measured with/without background activities representing the activities in the pig SPECT/CT scans.

The phantom dosimetry data based on multiple SPECT/CT images and based on multiple planar images in combination with one SPECT/CT scan (MP1S Imaging) were compared to the pig dosimetry. The calculated TIACs of the phantom with background based on multiple SPECT/CT and MP1S imaging were quite similar to the multiple SPECT/CT based pig TIAC.

In addition, in order to investigate the effect of late time points on dosimetry and absorbed dose values in ^{177}Lu therapies, the difference, associated with eliminating the late two scan time points, on the TIACs was analyzed. When the TIACs (including all time points) of the pig based on multiple SPECT/CT and MP1S imaging were investigated, the use of MP1S imaging results in considerably lower TIAC values to the kidney (by a factor of 1.4). With eliminating late time points from the created time activity curve, the factor increases up to 2.4 times with a corresponding increase in TIAC uncertainties.

As a consequence, further evaluation of ^{68}Ga-OPS202 for PET/CT imaging and ^{177}Lu-OPS201 for the treatments of NET patients is necessary. In particular, a head-to-head comparison of agonists and OPS peptides with respect to biokinetics, biodistribution and dosimetry would be helpful. In addition, the influence of the late scan time points on dosimetry needs further attention in particular for kidney dosimetry.

i. Zusammenfassung

Die Peptidrezeptor-Radionuklidtherapie (PRRT) beinhaltet die systemische Verabreichung von radioaktiv markierten Somatostatinrezeptor-bindende Peptiden. Sie zielt darauf ab, Rezeptoren, die in Tumoren überexprimiert sind, mit hoher Affinität und Spezifität anzusprechen. Es werden Peptide eingesetzt, die entweder als Agonist (mit Internalisierung) oder Antagonist (wenig bis gar keine Internalisierung) wirken. Vor kurzem wurden zwei neue antagonistische Wirkstoffe für den klinischen Einsatz entwickelt: OPS202 und OPS201. ^{68}Ga markiertes OPS202 wird für diagnostische Zwecke mit der Positronen-Emissions-Tomographie und ^{177}Lu markiertes OPS201 für die Therapie von Patienten mit neuroendokrinen Tumoren (NETs) verwendet. Beide Wirkstoffe befinden sich derzeit in der klinischen Erprobung. Trotz der sehr niedrigen Internalisierungsrate wird erwartet, dass der Einsatz von Somatostatinrezeptor-Antagonisten, die mehr Bindungsstellen an Rezeptoren ansprechen, zu einer höheren Spezifität, einer günstigeren Pharmakokinetik und einer höheren Tumorretention und besseren Visualisierung als die Agonisten führt.

Das Hauptziel dieser Arbeit war die Analyse der Biodistribution, Biokinetik und der internen Dosimetrie der neu entwickelten Somatostatinrezeptor-Antagonisten (OPS201 und OPS202) für therapeutische und diagnostische Zwecke in verschiedenen Spezies (Mäuse, Schweine und Patienten). Darüber hinaus wurde eine Analyse des Einflusses der Bildquantifizierung und der Integration von Zeitaktivitätskurven auf die Nierendosimetrie in einem Schweinemodell durchgeführt. Zudem wurden Extrapolationsmethoden, die zur Vorhersage der Energiedosen für das Blut, die Leber und die Nieren für den Menschen auf der Grundlage präklinischer Tiermodelle, die mit OPS201 injiziert wurden, systematisch verglichen.

Basierend auf den Patientenuntersuchungen mit OPS202 zeigt ^{68}Ga-OPS202 vielversprechende Biodistributions- und Abbildungseigenschaften mit einem Tumorkontrast, der eine Stunde nach Injektion des Radiotracers optimal ist. OPS202 ist gut verträglich; die Energiedosen in den Organen sind niedriger als die von ^{18}F-FDG und ähnlich wie andere ^{68}Ga-markierte Somatostatinrezeptorliganden. Nach einer Injektion von OPS202, das mit ^{68}Ga markiert wurde, wurden die höchsten Energiedosen in der Harnblase (0.10 mGy/MBq) und den Nieren (0.84 mGy/MBq) beobachtet. Der berechnete mittlere effektive Dosiskoeffizienten von Patienten, die mit ^{68}Ga-OPS202 injiziert wurden, betrug 0.024 mSv/MBq (3.6 mSv für 150 MBq ^{68}Ga-OPS202), ähnlich wie bei anderen ^{68}Ga-markierten Verbindungen.

Basierend auf den biokinetischen und dosimetrischen Untersuchungen von OPS201 wird nach der Injektion von ^{177}Lu-OPS201 in der ersten Phase (Halbwertszeit: 1.83 h) für jede Spezies eine schnelle Ausscheidung der Verbindung beobachtet. 10 Minuten nach der Injektion zirkulieren weniger als 5% der injizierten Aktivität pro Milliliter Blut bei Schweinen und Menschen.

Die Analyse der Daten von Mäusen, Schweinen und vorläufigen Patienten liefert Hinweise darauf, dass Patienten, die in eine ^{177}Lu-OPS201-Studie aufgenommen werden, nicht dem Risiko für eine Überexposition ausgesetzt wären.

Basierend auf unseren Ergebnissen werden für ^{177}Lu markierte Studien Nachbeobachtungszeiten insbesondere zu späten Zeitpunkten (mehr als 72 h) für die Berechnungen des zeitintegrierten Aktivitätskoeffizienten (TIAC) benötigt, um die Fläche unter der Kurve angemessen darzustellen und sowohl die Biokinetik als auch die Dosimetrie genau zu analysieren. Späte Zeitpunkte (nach 72 h) haben einen großen Einfluss auf die Berechnung der Energiedosis. Darüber hinaus wurden mehrere Extrapolationsmethoden vom Tier auf den Menschen getestet, um die geeignetsten Extrapolationsmethoden zu finden, die die Unterschiede zwischen den verschiedenen Spezies von Dosimetrie-Daten minimieren. Für OPS201 ergibt die Zeitskalierung oder die Kombination von relativer Masse und Zeitskalierung die ähnlichsten TIAC-Werte, wenn die Organmassenverhältnisse zwischen den Spezies hoch sind. Bei der Zeitskalierung wird die Scan-/Samplingzeit durch das Verhältnis der Ganzkörpermassen der jeweiligen Spezies skaliert. Bei der relativen Massenskalierung werden die TIACs basierend auf dem Verhältnis der Ganzkörper- und Organmasse der jeweiligen Spezies skaliert. Andere getestete Methoden zeigten höhere Abweichungen.

Um den Einfluss der Bildquantifizierung und die Wahl der optimalen Scanzeitpunkte zu untersuchen, wurde eine Studie in einem Schweinemodell, die in Zusammenarbeit mit der Universität Aalborg und der Octreopharm Sciences GmbH durchgeführt wurde, neu analysiert. Da die Nieren bei PRRT mit ^{177}Lu markierten Peptiden Risikoorgane sind, wurden mehrere Quantifizierungsmethoden ausgewählt, die auf 2D- und 3D-Bildgebung basieren. Zu diesem Zweck wurde ein 3D gedrucktes Schweine-Nierenphantom vorbereitet und, mit und ohne Hintergrundaktivitäten, die den Aktivitäten in den Schweinescans entsprechen, gemessen und quantifiziert,. Dosimetrie-Daten, die aus dem Schweinescan basierend auf mehreren 3D-Bildern und basierend auf mehreren 2D-Planarbildern in Kombination mit einem SPECT/CT-Bild („MP1S-Imaging“) gewonnen wurden, wurden mit den Ergebnissen der Phantomscans verglichen. Die so ermittelten TIACs des Phantoms mit Hintergrund, basierend auf beiden Bildgebungstechniken, entsprachen in etwa den Ergebnissen derjenigen Schweinedaten, die auf mehrfachen SPECT/CT-Aufnahmen basierten.

Um die Auswirkungen der späten Zeitpunkte auf die Dosimetrie und die Werte der Energiedosen in ^{177}Lu Therapien zu untersuchen, wurde außerdem der Unterschied, der mit der Eliminierung der späten zwei Scanzeitpunkte verbunden ist, auf die TIACs analysiert. Wenn auf mehreren SPECT/CT- und Hybrid-Bildern basierten TIACs des Schweins untersucht wurden, war die berechnete TIAC (einschließlich aller Zeitpunkte) basierend auf mehreren SPECT/CT-Bildern im Vergleich zur Hybrid-Imaging um den Faktor 1.4 höher. Durch die Eliminierung von späten Zeitpunkten aus der erstellten Zeitaktivitätskurve erhöht sich der TIAC um den Faktor 2.4 mit entsprechend höheren TIAC-Unsicherheiten.

Daher ist zu folgern, dass eine weitere Evaluierung von ^{68}Ga-OPS202 für die PET/CT-Bildgebung und ^{177}Lu-OPS201 für die Behandlung von NET-Patienten erforderlich ist. Insbesondere wäre ein direkter Vergleich von Agonisten und OPS-Peptiden in Bezug auf Biokinetik, Biodistribution und Dosimetrie hilfreich. Darüber hinaus bedarf der Einfluss der späten Zeitpunkte bei Dosimetrie-Scans weiterer Aufmerksamkeit, insbesondere bei der Nierendosimetrie.

1. Introduction

Recently, the somatostatin receptor subtype 2 (SSTR2) agonists as well as the antagonists have been used for imaging and treatment of neuroendocrine tumors (NETs) and gastroenteropancreatic neuroendocrine tumors (GEP-NETs) which are overexpressing the somatostatin receptor SSTR2. DOTA-[Tyr3]Octreotate (DOTATATE), DOTA-[Tyr3]Octreotide (DOTATOC), and DOTA-[NaI3]Octreotide (DOTANOC) are the agonists whereas the antagonists are OPS201 (DOTA-JR11, Cpac[D-Cys-Aph(Hor)-D-Aph(Cbm)-Lys-Thr-Cys]-D-Tyr-NH2)) and OPS202 (NODAGA-JR11) (*1-5*).
The recently introduced SST2 antagonists (OPS201 and OPS202), which, despite very low internalization rates, seem to recognize more binding sites on receptors and which show favorable pharmacokinetics and better tumor visualization than agonists, are the most important development in the field of SSTR2 targeting (*6*). Within the SSTR agonists and antagonists, DOTATATE has the European Medicines Agency's and the U.S. Food and Drug Administration's approval whereas DOTATOC has the U.S. Food and Drug Administration's approval (*7,8*). The recent developed antagonist JR11, or OPS, is under clinical development as a PET imaging agent when labeled with ^{68}Ga (^{68}Ga-NODAGA-JR11 or ^{68}Ga-OPS202,) and as a therapeutic agent when labeled with ^{177}Lu (^{177}Lu-DOTA-JR11 or ^{177}Lu-OPS201).

Based on the limited number of head-to-head comparisons of SSTR2 antagonists and agonists, previous preclinical and clinical studies have indicated that radiolabeled OPS antagonists are superior to the corresponding agonists especially for tumor targeting despite little to no internalization in tumor cells (*1,3,4,9,10*). OPS as an antagonist with high selectivity for SSTR2 shows the best overall characteristics for SSTR2 targeting and is therefore selected for clinical translation. The reason for these high selectivity characteristics is that the antagonistic peptides are independent of the somatostatin receptor activation state (G-protein phosphorylation). Therefore, they utilize more binding sites on the tumor cell surface, have a lower dissociation rate and also have longer tumor retention than agonistic peptides (*11*). It has also been shown that the uptake in the tumor is higher for SST2 antagonists compared to SST2 agonists (*1,3-5,11*). In contrast to the beneficial effect on tumors, there are also risks associated with peptide receptor radionuclide therapy (PRRT), mostly because of radiation toxicity to tumor-unaffected tissues, especially for the kidneys and the red bone marrow. To avoid treatment related side effects, dosimetry plays an important role on PRRT for each treatment cycle.

For individualized dosimetry, a variety of factors, such as size of the selected organs and tumors, uptake and tracer kinetics, should be carefully analyzed. Main focus in the patient-specific dosimetry is absorbed dose calculations of selected organs and organs-at-risk. For that purpose, accumulated activities in selected organs and organs-at-risk are evaluated based on drawn region of interests (ROIs) on 2D planar images and volume of interest (VOIs) on 3D SPECT/CT images. In 2D images, the overlap of neighboring regions or the disregarding of additional individual factors such as organ mass may lead to an incorrect determination of the ROI uptake, in turn resulting in an over- or underestimation of the absorbed dose in the corresponding region. In contrast, the use of multiple SPECT images in combination with a low-dose CT for morphological mapping and attenuation correction including scatter correction eliminates most of these problems and hence improves the dosimetry. As an alternative, since having SPECT/CT scans at multiple time points after administration of the therapeutic radiopharmaceutical is not common in the clinical routine of most departments, combining one SPECT/CT with multiple planar images can be a compromise to achieve the best possible dosimetry (*12*). There is no published study in the literature that shows the difference on dosimetry or distinguishes the accuracy between using multiple SPECT/CT scans and using multiple planar images plus one SPECT/CT (at identical time point of one planar image). As a part of this thesis, the optimal way for dosimetry and the accuracy of used image modalities was investigated.

In total, there is one clinical paper (*4*), two preclinical mouse model publication (*3,9*), and one preclinical pig study (*2*) with ^{177}Lu-OPS201. In these studies, the main focus was on either the biodistribution or dosimetry. In the clinical study by Wild et al. (*4*), the dosimetry of four patients with advanced NET was analyzed and compared to ^{177}Lu-DOTATATE. In the preclinical study by Dalm et al. (*9*), tumor xenografted mice were used to determine the optimal dosage for therapy and the therapeutic effect of ^{177}Lu-DOTA-JR11 was compared to ^{177}Lu-DOTA-octreotate. However, the counting time points and intervals of the experiments after the mice were euthanized were not sufficient (4 h, 2 d, 4 d, and 7 days after injection) for an accurate quantification of the biodistribution and dosimetry. In another preclinical study on mice by Nicolas et al. (*3*), OPS201 labeled with ^{177}Lu, ^{90}Y, and ^{111}In and was compared with the ^{177}Lu-DOTATATE. Neither time-integrated activity coefficient (TIAC) values nor absorbed dose values were reported. Instead, only the relative administered activity values per gram were reported.

In the preclinical pig study by Beykan et al. (*2*), the focus was on in vivo biodistribution and dosimetry. Five pigs were analyzed, TIACs, absorbed doses and effective dose coefficient values were reported. It was mentioned that, in preclinical studies, rodents are the most frequently used species. However, larger animals such as pigs or dogs are expected to mimic human physiology better than rodents (*2*). These larger animals can be scanned several times with a human SPECT/CT under very similar conditions as patients. Therefore, these studies have the advantage of long follow up times and that multiple blood samples can be taken for dosimetry and metabolism assessment similar to patient studies. However, there can still be different biokinetics between species. As it is reported in the paper by Beykan et al. (*2*), pigs have a spine uptake in comparison to humans where no ^{177}Lu-OPS201 spine uptake occurred. None of the preclinical studies in the literature accommodated methods neither for absorbed dose calculations nor for considering the differences in physiology between animals and humans. For this reason, extrapolation methods that are based on mathematical equations in order to predict TIACs and, consequently, absorbed doses in humans by using data collected from animals must be applied in preclinical studies. Most importantly, these techniques are needed for predicting the absorbed doses for a first application of any newly developed radiopharmaceutical in humans (*13*). As of today, there is no systematic study that analyzes the difference in biokinetics of radiopharmaceuticals dedicated to therapy between animal models and patients. In total, there are five published interspecies extrapolation methods related to the use of radionuclides (*13,14*) in preclinical studies. However, there are no published studies either comparing these extrapolation methods or optimizing a scaling method. Therefore, another goal of this thesis was a test of all published methods to determine an adequate scaling method of preclinical studies. The results of the investigation was published in 2019 (*6*).

There are currently three published clinical papers related to ^{68}Ga-OPS202 (*15-17*). In the study by Nicolas and Beykan et al. (*15*), the main focus was on biodistribution, radiation dosimetry and feasibility of using OPS202 for PET imaging of NETs while the main focus in the study in 2018 by Nicolas et al. (*16*) was lesion contrast, lesion detection, and a sensitivity comparison between ^{68}Ga-OPS202 and ^{68}Ga-DOTATOC patients with GEP-NETs. In the study by Nicolas et al. (*16*), neither absorbed dose values (mGy/MBq) nor effective dose coefficient (mSv/MBq) values were published.

In another clinical study by Krebs et al. (*17*), the main focus was on biodistribution and radiation dose estimations. They reported absorbed dose values and effective dose coefficient value for the six selected patients based on only two PET scans and they did not report time activity curves. Although they reported similar mean effective dose coefficient value to the paper by Nicolas and Beykan, et al.(*15*), the temporal arrangement as well as the number of time points for the PET/CT scans (no late scan time points) were insufficient for an accurate quantification of the biodistribution and dosimetry of OPS202.

The main goal of the thesis was to analyze the biodistribution, biokinetics and internal dosimetry of somatostatin receptor antagonists in ^{177}Lu-OPS201 injected species (mice, pigs and humans) for therapy and ^{68}Ga-OPS202 injected patients for diagnostics. OPS201 data were obtained as described by the study of Nicolas et al. (for mice (*3*)), of Beykan et al. (for pigs (*2*)) and of Wild et al. (for humans (*4*)). OPS202 data for patients were taken from the study by Nicolas et al. (*15*)). In addition these investigations, all published extrapolation methods related to the use of radionuclides ("scaling methods") were examined on ^{177}Lu-OPS201 injected animals in order to find the optimal method for analyzing biokinetics and dosimetry for preclinical studies. Another goal of the study was to compare 2D and 3D quantitative imaging modalities by using a 3D-printed phantom to find an optimal way to calculate kidney absorbed dose values more accurately in ^{177}Lu labelled therapies. In the majority of publications, estimating kidney absorbed doses is based on 2D planar imaging. An alternative way for estimating kidney absorbed doses is either the use of multiple 3D images or the use of multiple 2D planar images in combination with one 3D image. One of the pig data sets of the OPS201 pig study (*2*) and a 3D-printed phantom, corresponding pig kidney, were used to compare these imaging techniques for kidney dosimetry. The advantage of using the pig study was that planar and whole-body SPECT/CT images were taken over a period of almost 300 hours. For both pig and phantom data set, TIACs and fit parameters based on multiple SPECT/CT and multiple planar images plus one SPECT/CT scans were calculated separately and compared. In addition, in order to show the effect of late activity measurements post-injection time points on dosimetry and absorbed dose values, the difference in TIACs calculated using NUKDOS (*18*) was investigated with eliminating the last two scan time points.

2. Background

2.1. Radiation

Radiation is an energy that comes from a source and travels through some material or through space such as light, heat or sound. Radiation can be classified as ionizing and non-ionizing. Non-ionizing radiation has longer wavelength, lower frequency and, therefore, lower energy than ionizing radiation (shorter wavelength, higher frequency, higher energy). The ionization energy is the amount of energy needed to release an electron from the neutral atom. There are two different types of ionizing radiation, either directly by charged particles or indirectly by neutral particles. Directly ionizing radiation deposits energy in the medium through direct Coulomb interactions between the ionizing charged particle and orbital electrons of atoms in the medium. Indirectly ionizing radiation deposits energy in the medium through a two-step process. First of all, a charged particle is released in the medium. For instance, photons release electrons or positrons while neutrons release protons or heavier ions. Secondly, the released charged particles deposit energy to the medium through direct Coulomb interactions with orbital electrons of the atoms comprising the medium. The types of indirectly ionizing radiation by photons can be classified as ultraviolet light, characteristic X-rays, γ rays and annihilation radiation (*19*).

2.2. Characteristic X-rays

Characteristic X-rays are emitted through electron-nucleus interactions. X-rays for medical diagnostic procedures or research purposes are produced by accelerating electrons with high voltage in order to allow them to collide with a metal target. When the electrons suddenly decelerate upon collision with the metal target, they lose their energy. If the accelerated electrons have sufficient energy, they can remove an electron from the inner shell of the target metal atoms. As a consequence, the electrons from higher energy states fill the vacancy. In this process, the energy difference is released as X-rays, also called characteristic X-rays.

2.3. Radioactive Decay

Radioactive decay is the process in which an unstable atomic nucleus loses energy by emitting radiation in the form of particles or electromagnetic waves. The unstable nucleus is transferred into more stable entities until a stable nuclear configuration is reached. A radioactive parent X with atomic number Z and atomic mass A can decay into a daughter Y through the possible modes of decays such as α, β^-, $\beta^+\gamma$, electron capture and internal conversion (*19*).

α Decay: it occurs when an atomic nucleus emits an ${}_2^4He$ particle referred to as an α particle.

$${}_Z^AX \rightarrow {}_{Z-2}^{A-4}Y + {}_2^4He \qquad \text{Eq.2.3.1}$$

β^- Decay: A neutron transforms into a proton, an electron (β^-) and antineutrino $\bar{\nu}e$, sharing the available energy, are ejected from the nucleus.

$${}_Z^AX \rightarrow {}_{Z+1}^{A}Y + \beta^- + \bar{\nu}e \qquad \text{Eq.2.3.2}$$

β^+ Decay: A proton transforms into a neutron, a positron β^+ and neutrino νe, sharing the available energy, are ejected from the nucleus.

$${}_Z^AX \rightarrow {}_{Z-1}^{A}Y + \beta^+ + \nu e \qquad \text{Eq.2.3.3}$$

γ Decay: An excited nucleus ${}_Z^AX^*$, generally produced through β^- or β^+decay, reaches its ground state ${}_Z^AX$ through emission of one or several γ photons.

$${}_Z^AX^* \rightarrow {}_Z^AX + \gamma \qquad \text{Eq.2.3.4}$$

Internal conversion: Rather than being emitted as a γ photon, the nuclear excitation energy may be transferred to a K, L, M shell orbital electron that is ejected with a kinetic energy equal to the excitation energy less the orbital electron binding energy. The resulting K, L, M shell vacancy is filled with a higher level orbital electron and the transition energy is emitted in the form of characteristic photons or Auger electrons.

$${}_Z^AX^* \rightarrow {}_Z^AX + e_{K,L,M}^- \qquad \text{Eq.2.3.5}$$

A radionuclide decays by losing energy. The time which takes for half of the atoms to decay is called half-life ($T_{1/2}$) of the specific radionuclide. This decaying process continues until the number of atoms of the radionuclide eventually reached to the zero value. The decay process is described by the decay equation:

$$A(t) = A(0) \cdot e^{-\lambda t} = A \cdot e^{-\frac{ln2}{T_{1/2}} \cdot t} \qquad \text{Eq.2.3.6}$$

Where $A(t)$ and $A(0)$ is the amount of radioactivity in an initial and certain time point respectively, λ is the radionuclide-specific decay constant, $T_{1/2}$ is the half-life of the radionuclide and t is the time difference between the first and last time point (*19*).

The amount of radioactivity caused by any radionuclide is defined as the number of decays per time. The SI unit of radioactivity is the Becquerel (Bq). One Becquerel is defined as one radioactive decay per second. A related term, in nuclear medicine, is count which refers to the registration of a single decay by a detector (*20*). Detectors used in nuclear medicine detect only the fractions of the decays, principally as the radiation from many of the decays is directed away from the detector. Count rate refers to the number of decays actually counted in a certain time. The number of counts acquired during the image frame is proportional to the amount of the injected radionuclide activity. The important correction that needs to be applied in clinical applications is removing the effects of physical decay by decay correcting based on accounting the injection time and the time that the syringe were measured in the dose calibrator.

2.4. Emission Computed Tomography

Tomography is the process of collecting data about an object from multiple views, and using these data to reconstruct a set of images of, the so-called “slices”, through the object. In Computed Tomography (CT), a computer is used to reconstruct an image of the patient from multiple views. A similar type of study can be performed in nuclear medicine by detecting photons emitted from a radiopharmaceutical distributed within the body. This method is called emission computed tomography. Production of tomographic images by detection of annihilation photons released during β+ decay is referred to as positron emission tomography (PET) whereas tomographic images computed from the registration of interactions of individual γ rays in a crystal is referred to as single-photon emission computed tomography (SPECT).

2.5. SPECT/CT Imaging Technique

SPECT/CT consists of a gamma camera which produces a functional 3D distribution of a photon emitting radionuclide inside the body combined with a CT, which uses an external source of X-rays, to produce anatomical 3D images. The camera rotates either continuously or in fixed angle steps around the object normally in a full 360° turn. SPECT/CT cameras provide a combination of functional and anatomical images. In SPECT/CT, X-rays from a CT scan are additionally used to obtain an attenuation map and with the help of this map, the attenuation correction can be performed for correcting for the absorption of the emitted photons. The attenuation map can be easily integrated into reconstruction algorithms for SPECT/CT images. A SPECT study consists of two parts: acquisition and reconstruction.

2.5.1. Acquisition

Acquisition is the process of detecting photons caused by ionizing radiation and converting the detected photons into electrical or optical or other signals with subsequent spectroscopic counting. The detected photon data represents the sum of the attenuation of all tissues that the photons have passed through which is a 2D array of data containing the projections. The detected photon data is named as raw data or a sinogram. During acquisition, the detector system rotates around the patient so that many different angular views or projections of the patient are obtained. Higher number of counts result in better counting statistics, which can be considered as better image quality. However, to acquire a higher number of counts from the same source, one has to use a longer acquisition time, in turn increasing the possibility of artifacts due to patient motion. To optimize the acquisition time, multiple detectors can be used. Currently, the typical SPECT systems are equipped with two camera heads.

2.5.2. Reconstruction

In the tomographic reconstruction process, the sinograms are used to generate a 3D image volume of the scanned object. There are 2D and 3D iterative reconstruction methods such as 2D ordered subset expectation maximization (OSEM).

The general concept of iterative reconstructions is outlined in figure 2.5.2. In essence, the algorithm approaches the true image, I , by means of successive estimates denoted by I^*. The next step (called the inverse of back projection) is to compute the projections that would have been measured for the estimated image, using a process called forward projection. It is performed by summing up the intensities along the potential ray paths for all projections through the estimated image. The set of projections generated from the estimated image then is compared with the actually acquired projections. The difference between the estimated and the actual projections is used to adjust the estimated image to achieve a closer agreement. The update-and-compare process is repeated until the difference between the forward-projected profiles for the estimated image and the actually recorded profiles falls as possible as minimum level. With proper design of the image updating procedure, the estimated image progressively converges toward the true image (*21*).

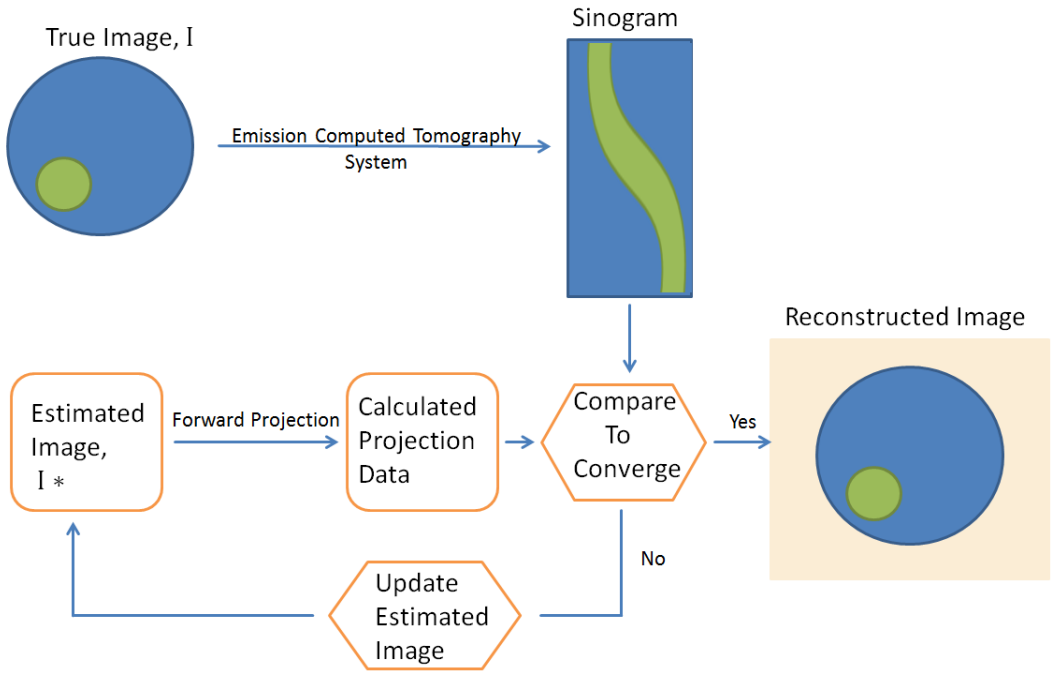

Figure 2.5.2: The Steps in Iterative Reconstruction (based on (*21*))

[An initial image estimate is made and projections that would have been recorded from the initial estimate then are calculated by forward projection. The calculated forward projection profiles for the estimated image are compared to the profiles actually recorded from the object and the difference is used to modify the estimated image to provide a closer match. The process is repeated until the difference between the calculated profiles for successively estimated images and the actually observed profiles reaches some acceptably small level.]

2.5.3. Resolution and Partial Volume Effect

In SPECT, the spatially variant collimator detector response significantly degrades spatial resolution and creates significant partial volume effects (PVEs) for small objects. The full width at half maximum of the collimator-detector response function increases approximately in proportion to the distance from the collimator. As a result, SPECT/CT images have a spatially varying spatial resolution. This means that PVEs will be spatially varying and the accuracy of quantifying small objects will thus be position-dependent. In general, the tangential resolution improves away from the center of rotation, while the radial resolution is almost constant (*22*).

2.6. Somatostatin Receptors and Somatostatin Receptor Analogs

In total five G-protein coupled somatostatin receptor subtypes (SSTR1-5) have been identified for humans. Each SSTR are differentially expressed throughout the central nervous system and the periphery (including kidneys, pancreas and gastrointestinal tract). Their overexpression especially in neuroendocrine tumors (NETs) makes them useful for both diagnostic and therapeutic purposes in the clinic. The interest of using SSTR targeting with radionuclide labeled agonistic and antagonistic analogs in nuclear medicine for diagnostic purposes, tumor staging and therapeutic purposes (peptide receptor radionuclide therapy, PRRT) is increasing year by year. The main difference between agonists and antagonists is the internalization phase (in other words, the cell activation stage), which can be seen in figure 2.6.1. Agonists only target activated receptors whereas antagonists are independent of the somatostatin receptor activation state (G-protein phosphorylation). After the injection of radionuclide labelled antagonists or agonists, the concentration into the NETs sites occur and the radionuclide labeled peptides bind to SSTR2 overexpressed by NETs. At that stage, the only difference is that agonists are internalized in the NET cells while there is little to no internalization for antagonists in order to deliver radiation to the cancer cells. Therefore, antagonists utilize many more binding sites on the tumor cell surface. Due to their superior binding behavior, with using antagonists smaller lesions can be detected, longer tumor retention is observed and also higher tumor uptake is achieved (*1,4,11*). The chemical structures and binding affinities of both agonistic and antagonistic peptides based on the literature is summarized in table 2.6.1 (*7*). As a result, the radiation related to agonistic and antagonistic peptides labeled with radionuclide induces DNA strand breaks causing tumor cell death.

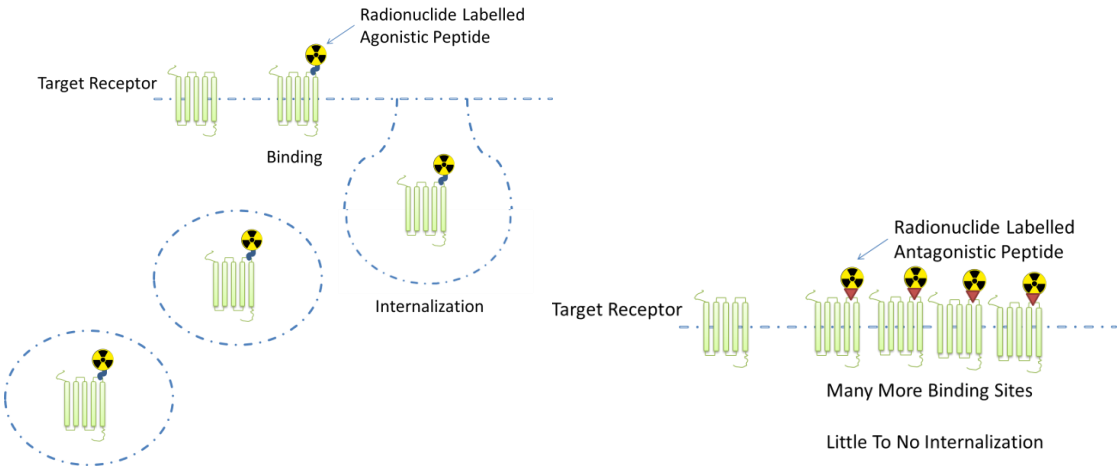

Figure 2.6.1: Mechanism Difference between Agonistic and Antagonistic peptides (based on (*11,23*))

Somatostatin Analogue		Affinity (nM)				
		SSTR 1	SSTR 2	SSTR 3	SSTR 4	SSTR 5
Agonists	^{111}In-DTPA-Octreotide	>10^4	22	182	>10^3	237
	^{68}Ga-DOTATOC	>10^4	2.5	613	>10^3	73
	^{90}Y-DOTATOC	>10^4	11	389	>10^4	114
	^{68}Ga-DOTATATE	>10^4	0.2	>10^3	300	377
	^{90}Y-DOTATATE	>10^4	1.6	>10^3	523	187
	^{177}Lu-DOTATATE	>10^3	2.0	162	>10^3	>10^3
	^{68}Ga-DOTANOC	>10^4	1.9	40	260	7.2
Antagonists	In-DOTA-BASS	>10^3	9.4	>10^3	380	>10^3
	In-DOTA-JR11	>10^3	3.8	>10^3	>10^3	>10^3
	Ga-DOTA-JR11 (Ga-OPS201)	>10^3	29	>10^3	>10^3	>10^3
	Ga-NODAGA-JR11 (Ga-OPS202)	>10^3	1.2	>10^3	>10^3	>10^3
	Lu-DOTA-JR11 (Lu-OPS201)	>10^3	0.7	>10^3	>10^3	>10^3

Table2.6.1: Somatostatin Analogue Affinity Table (Based on (*7*))

2.7. Radionuclides Used for Imaging and Therapy in Clinic

The radionuclide selection must be based on the appropriate emission type and half-life that is required for the specific clinical situation. For instance, the physical decay constant of the radionuclide used for diagnostic imaging must be similar to the uptake rate and washout of the used radiopharmaceutical. Otherwise, selected short half-life radionuclide will decay before the radiopharmaceutical reaches the target or selected long half-life radionuclide will remain in the patient longer than necessary and deliver the unnecessary radiation.

In medicine, decays with α and β^- radiation are used for treating diseases such as cancer while decay with β^+ and γ radiation are used in conjunction with medical scanners and cameras for diagnostic purposes. The most common radionuclides relevant for PET and SPECT imaging and molecular radiotherapy (*24*) and some of their properties are shown in table 2.7.1.

Radionuclide	Half-life (h)	Radiation Emission (Probability)	Production
Positron emitters (PET radionuclides)			
^{11}C	0.34	β^+ (100%)	Cyclotron
^{18}F	1.83	β^+ (97%)	Cyclotron
^{64}Cu	12.8	β^+ (19%)	Cyclotron
^{68}Ga	1.13	β^+ (89%)	Generator
^{89}Zr	78.4	β^+ (23%)	Cyclotron
^{124}I	100	β^+ (23%)	Cyclotron
Gamma emitters (SPECT radionuclides)			
^{123}I	13.2	γ (83%)	Cyclotron
^{99m}Tc	6	γ (89%)	Generator
^{111}In	67.9	γ (185%)	Cyclotron
Therapeutic radionuclides			
^{90}Y	64	β^- (100%)	Generator
^{131}I	192	β^- (100%)	Fission
^{177}Lu	160	β^- (100%)	Reactor

Table 2.7.1: Selected Radionuclides Used in Clinical PET, SPECT and Radiotherapy, Their Production Mode and Decay Properties (Based on http://www.lnhb.fr/nuclear-data/nuclear-data-table/)

The radionuclides used in the thesis are ^{68}Ga and ^{177}Lu. The physical properties of these two radionuclides are explained in detailed in the following paragraphs.

2.7.1. Properties of ^{68}Ga

The radionuclide ^{68}Ga is a generator-produced radionuclide from a source of Germanium-68 (^{68}Ge). ^{68}Ge decays solely by orbital electron capture to ^{68}Ga (half-life of 1.13 hours). The latter disintegrates to 89% by the emission of β^+ of 1.9 MeV maximum energy and to 11% by electron capture to stable Zinc-68 (^{68}Zn). Not only its β^+ emission, also the physical and chemical properties of ^{68}Ga make it suitable for PET imaging (*25*). The high positron emission fraction (89%, Emax: 1899 keV, Emean: 890 keV) and the half-life of 1.13 hours provide high quality images while minimizing radiation dose to the patient and personnel (*26*). On the other hand, ^{68}Ga with its rather high positron energy is expected to have lower resolution compared to ^{18}F, however both a computational analysis and experimental measurements demonstrated equally high quality images for these two radionuclides assuming a scanner detector resolution of 3 mm (*25*).

2.7.2. Properties of ^{177}Lu

The radionuclide ^{177}Lu has a 6.65 days half-life and disintegrates by beta-emission (probability: 100%) to the ground state and to the three excited levels of ^{177}Hf. The maximum beta-energy is 498 keV. There are two main gamma emissions that have photon energies of 208.3 keV with a probability of 10.38% per disintegration and 112.9 keV (6.2%). ^{177}Lu-labelled compounds show many advantages for dosimetry assessments due to attractive physical properties which comprise low abundance of photons, sufficient for post-therapy imaging and a clearly separated gamma peak at 208.3 keV. Due to its' low photon emission probability, even a 7 GBq therapeutic activity injection allows post-therapeutic imaging with negligible camera dead-time effects (*27*).

2.8. Peptide Receptor Radionuclide Therapy (PRRT) for NET

Peptide receptor radionuclide therapy (PRRT) is a molecular radiation therapy (also called targeted radionuclide therapy). It involves the systemic administration of a radiolabeled peptide designed to target, with high affinity and specificity, receptors overexpressed on tumors (*28*). The PRRT is applied with using either agonist or antagonist peptides. In the PRRT treatment, the used radionuclide chelated to the either agonist or antagonist ligands via a linker. While the radionuclide emits electrons and/or photons which are useful for therapeutic and imaging purposes, respectively, the peptide targets to the somatostatin receptors overexpressed by tumors. Based on the used SSTR peptide with internalization (for agonists) or without internalization (for antagonists) radiation is delivered to the tumor cells. A schematic overview of targeted peptide receptor radionuclide is shown in figure 2.8.1.

In PRRT, the bone marrow and kidneys are the organs at risk. Since amino acid infusion results in a significant reduction of the kidney absorbed dose values, amino acid infusion (at least 30 s prior to the radionuclide injection) is applied to the patients as part of the treatment protocol in order to protect the kidneys (*28*). As it is a main goal in each treatment in nuclear medicine, to minimize the absorbed dose delivered to normal organs while achieving high uptakes in tumors, performing patient specific dosimetry would be optimal.

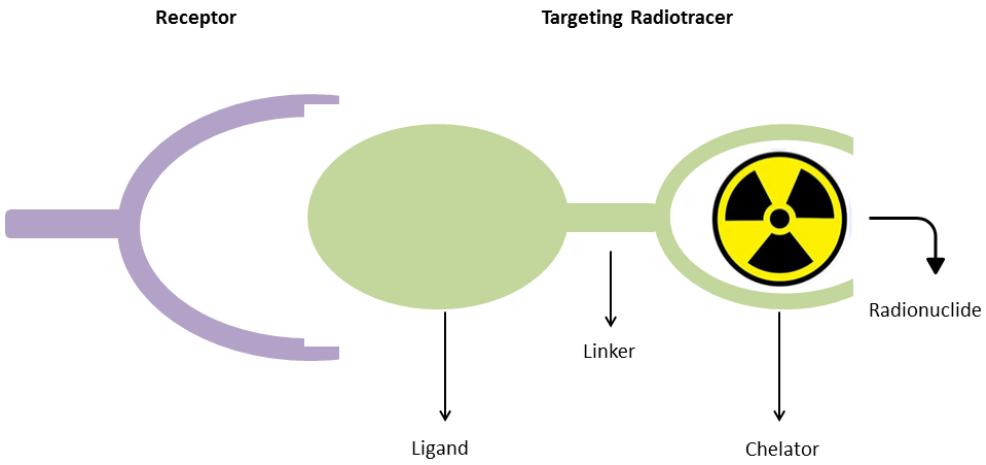

Figure 2.8.1: Schematic Overview of Targeted Peptide Receptor Radionuclide

[The chelator enables labeling the ligand with radionuclides that enables both imaging and therapy.]

2.9. OPS201/202 Labelled Therapeutic and Diagnostic Radiopharmaceuticals

2.9.1. ^{177}Lu Labelled OPS201 Peptide for Therapy

As in other molecular radiation therapy in nuclear medicine, the ^{177}Lu-OPS201 treatment can be applied based on either the empiric fixed activity treatment protocol (7.4 GBq per cycle) or the personalized, patient-specific, treatment protocol for each therapy cycle. Current studies showed that a personalized protocol resulted in an increase in the cumulative maximum tumor absorbed dose compared to empiric PRRT(*29*). In addition, patient-specific treatments have a positive impact as they show lower uptake in normal healthy tissues and it reduces the concentration of the therapeutic radiopharmaceutical in excretory organs such as the kidneys in comparison to empiric treatments (*30*).

The therapeutic antagonist, ^{177}Lu-OPS201, resulted in 1.7- to 10.6-fold higher tumor doses than the SSTR agonist ^{177}Lu-DOTA-TATE in four patients with metastatic NET (*4*). In addition, ^{177}Lu-OPS201 exhibited higher tumor uptake, longer tumor retention, and an improved tumor-to-kidney dose ratio compared to ^{177}Lu-DOTA-TATE and ^{90}Y-OPS201 (*29*). These findings were sufficient to initiate an international multi-center, open-label study which started in March 2017 with an estimated completion in May 2022, to evaluate the safety, tolerability, biodistribution, dosimetry and preliminary efficacy of ^{177}Lu-OPS201 (ClinicalTrials.gov identifier: NCT02592707) in patients with SSTR-positive NET. The evaluation of the theranostic pair ^{68}Ga-OPS202 and ^{177}Lu-OPS201 in patients with SSTR-positive NETs, is currently ongoing in a single center study (ClinicalTrials.gov identifier: NCT02609737) (*29*).

2.9.2. ^{68}Ga Labelled OPS202 for Diagnostic Imaging

There are currently 3 clinical studies with OPS202 labeled ^{68}Ga ((*15*),(*16*),(*17*)). In the study by Nicolas, Beykan, et al. (*15*) in 2018 the main focus was on biodistribution, radiation dosimetry and feasibility of using OPS for PET imaging of NETs while the main focus in the 2018 study by Nicolas et al. (*16*) was lesion contrast, detection, and sensitivity comparison between ^{68}Ga-OPS202 and ^{68}Ga-DOTATOC patients with gastroenteropancreatic neuroendocrine tumors (GEP-NETs). In another clinical study in 2019 by Krebs et al. (*17*), the main focus was on biodistribution and radiation dose estimations. Based on these studies, high tumor-to-background ratios and rapid blood clearance was observed. Not only all reported mean effective dose coefficients were similar to other ^{68}Ga labelled compounds but also the antagonistic shows significantly higher lesion-based overall sensitivity than the agonist-based scans (94% and 88% for 50 μg of peptide and 15 μg ^{68}Ga-OPS202 and 59% for 15 μg ^{68}Ga-DOTATOC, respectively)(*29*).

2.10. Dosimetry in Nuclear Medicine

2.10.1. General Concept of Dosimetry in Nuclear Medicine

For dosimetry in nuclear medicine, either blood sampling or 2D planar images or 3D PET/CT and 3D SPEC/CT images are used to analyze the amount of cumulated activity and biodistribution after activity injection. Analysis of region of interests (ROIs) for planar images and volume of interests (VOIs) for PET/CT and 3D SPEC/CT images are required for the selected organs in each scan time points. With the information coming from ROIs, and VOIs, the percentage of administered activity of the radiopharmaceutical for the accumulating organs must be calculated to create time activity curves. Then the time activity curves must be integrated by using an optimal fit function in order to calculate time-integrated activity coefficient values (TIACs, $\widetilde{\alpha}$ in Eq.2.10.1) for the selected organs. The calculated TIACs are used to calculate absorbed dose ($\overline{D}$) values for selected organs. The absorbed dose ($\overline{D}$) value of an organ is defined as (*31,32*):

$$\overline{D} = \widetilde{\alpha} \cdot A_0 \cdot S \qquad \text{Eq.2.10.1}$$

Where S is the radionuclide-specific quantity representing the mean absorbed dose rate to target tissue at time t after administration per unit activity present in the source tissue and A_0 represent the administered activity (*32*).

As a basis for the calculation of absorbed doses, the number of decays per administered activity must be determined for each organ or voxel or even on a cellular level. There are different dose calculation based on absorbed dose rates per unit activity (with mass correction) of anthropomorphic phantoms, convolution kernels, or Monte-Carlo simulations (*27*).

The majority of limitations and uncertainties of dosimetry in nuclear medicine can be attributed to image degradation, calibration of system sensitivity, VOI/ROI delineation, partial volume effects, precise determination of organ/lesion volumes (the use of standard organ volumes may be severely incorrect, leading to serious under- or overdosing in targeted radiotherapy), organ activity overlay, reconstruction settings, attenuation and scatter correction, filtering, suboptimal sampling and scan time points, image registration curve fitting, integration and dose conversion (*27,33*). In addition, for accurate dosimetry based on quantitative imaging, the reconstruction parameter, the energy window settings, the collimator, the scan duration and the applied corrections must be identical for each scan time.

2.10.2. Influence of the Reconstruction Parameters on Image Quantification with SPECT/CT

The applied reconstruction algorithm plays a significant role on image quantification of SPECT/CT. The choice of reconstruction parameters (such as number of iteration/subsets and filtering) is a compromise between image noise and resolution. For OSEM-based iterative reconstruction algorithms, an increase in number of subsets and applied iterations improves the spatial resolution of the image, but at the same time increases the image noise (*22,34*). Therefore, for optimal visibility of lesions and organs, it is recommended to investigate this dependency and optimize reconstruction parameters using a sample patient data set with representative activity distributions and counting statistics (*35*).

In addition, applied filters on reconstructed images can result in either an underestimation or overestimation of counts in the volume or region of interest. For instance, according to the published paper in 2019 (*34*), the activity calculated based on filtered reconstructed images was underestimated compared to applied unfiltered reconstructions. Also applied post-reconstruction filters such as Gaussian filtering may influence activity calculation and also have an effect on the partial volume effect which is directly related to visibility which may affect not only dosimetry but also diagnostics in a great range (*34*).

2.10.3. SPECT/CT Attenuation and Scatter Correction, Energy Window and Collimator Choice

In SPECT/CT, a low-dose CT scan is used to generate an attenuation map. Based on this map, attenuation correction can be performed for correcting for the absorption of the emitted photons. The attenuation map can be easily integrated into iterative reconstruction techniques for SPECT imaging. Attenuation is a depth-dependent property. Therefore, images which are not corrected for attenuation result in underestimations of activities especially in regions located deep in the body. In other words, the attenuation correction adds counts back into the areas where the activities are underestimated mainly due to photons absorption related to the surrounding tissues.

Similar to attenuation, the scattered-to-primary-photon ratio increases approximately linearly with source depth, so the quantitative effects of scatter are larger for source positions near the center of the object. Due to scattered photons in the projection data, the reconstructed image exhibits a spatially varying overestimation of activity in the order of 20-50% depending on the position. Therefore, applying proper scatter correction plays an important role for the accurate activity determination (*22,36*).

In addition, a proper energy windows setting must be chosen based on the main photo-peak of the used radionuclide in order to have less effects of scatter. Also the choice of collimation in combination with the energy window range is important since they affect sensitivity and spatial resolution (*22*). The collimator must be chosen to ensure high system sensitivity, to achieve a good signal-to-noise ratio and to minimize septal penetration of high-energy photons. If the collimator septa are not thick enough, photons which penetrate or scatter in the collimator septa will be detected, resulting in decreased image contrast, degradation of spatial resolution and increased image artifacts (*35*).

2.10.4. Calibration Factor (System Sensitivity) Calculation

Reconstructed images represent the distribution of emitted photons as the number of counts in each pixel or voxel. To convert counts to activity, the camera system must be carefully calibrated by using a radioactive source with a well-determined activity in combination with the same collimator, energy window and reconstruction settings as used in patient scans (*35*). A radioactive point source and a radioactive cylindrical source are the two main approaches used to calculate the calibration factor. For the method using a cylindrical phantom, a large water cylinder containing a well-calibrated source of radionuclide (such as ^{177}Lu) must be scanned by using the same acquisition protocol, corrections, and reconstruction as used in patients. The calibration factor (Eq. 2.10.2.) is then determined by dividing the total counts in the reconstructed image of the phantom by the acquisition duration and activity (*35*). It is important to mention that a calibration of the system sensitivity needs to be performed for each type of collimator, radionuclide, energy window setting and for each set of applied scan parameters. Depending on the type of acquisition, calibration factors need to be measured for corresponding acquisition protocols (*22*). Mathematically, the calibration factor or system sensitivity has the unit counts-per-second-per-MBq and is described by:

$$\text{Calibration Factor} = \frac{\text{Counts [c]}}{\text{Acquisition Duration [s]} \cdot \text{Activity [MBq]}} \qquad \text{Eq.2.10.2}$$

2.10.5. Activity Determination

For the selected organs in each scan time points, the information coming from drawn ROIs on planar images and/or VOIs on PET/CT and 3D SPEC/CT images is converted to percentage of administered activity in the organ by using the calibration factor.

ROIs on planar images are defined from anterior and posterior views. ROIs for the selected organs must be drawn with avoiding overlays as much as possible (See figure 2.10.6). For each selected regions, background ROIs must be also drawn for the background correction since there are always scattered radiation from other organs. The background ROI (Green ROI) must be drawn close to the main ROI in order to represent the activity of nearby tissues to the main ROI (Blue ROI). Then the background counts, associated with spill-in from neighboring organs, are subtracted from the main ROI in order to calculate the counts in the main ROI. To quantify the organ uptake, ROI for WB (Red ROI) including the whole patient body and a ROI for the background of the WB (Orange ROI) must also be drawn and analyzed. If the areas of the drawn ROIs are not exactly the same, the normalization is required before background-correction.

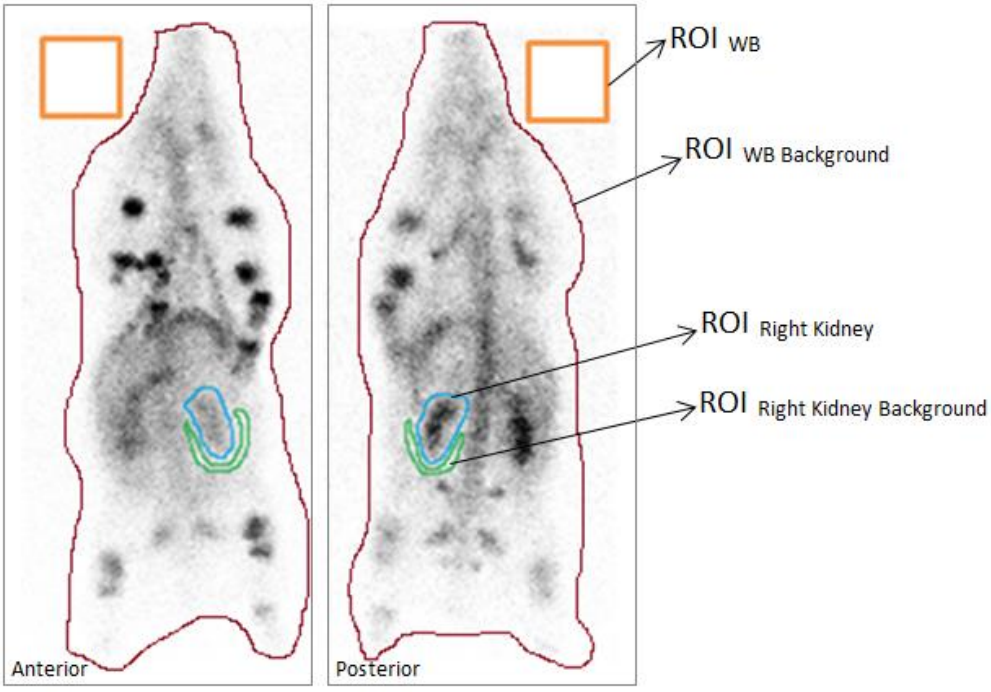

Figure 2.10.6: Anterior and Posterior Views of Planar Image of a Pig

[Blue and red ROIs represent the right kidney and the whole body (WB) region respectively. The background regions of right kidney and WB are represented by green and orange ROIs, the Whole body (WB) region (Red ROI) and the WB background region (ROI).]

After applying corrections on anterior and posterior counts, the geometric-mean method which is widely used for activity quantification of planar images for dosimetry calculations can be applied. The geometric mean of counts was obtained from drawn ROIs in the anterior and the posterior views. The geometric mean counts for the drawn ROI can be defined as the Eq. 2.10.3 (*37*).

$$\text{Geometric Mean}_{\text{ROI}} = \sqrt{C_A \cdot C_P} \qquad \text{Eq.2.10.3}$$

Where C_A: total anterior counts, C_P: total posterior counts.

As a last step, the calculated count values for the drawn organ can be converted to the percentage of administered activity values in each scan time point either by using a calibration factor or with the assumption of setting the whole-body uptake to 100% at the first scan time point just after injection.
The most critical issue while drawing ROIs on planar images is organ overlay. This may lead to either underestimations or over estimations in counts for the selected region. Also regions where spill-in or spill-out occurs due to the limited spatial resolution must be considered carefully.
In addition, especially due to organ overlay, it is recommended to perform activity determination based on SPECT/CT and PET/CT images.

VOI delineation on 3D images should be performed based on CT with avoiding spill-out effect as much as possible (see Figure 2.10.7). (*22*). In order to avoid spill-out effects, CT-based organs VOIs were enlarged at least as matching 2 voxel plus their actual CT-based volumes. To convert counts to activity (Eq. 2.10.4), the camera system must be carefully calibrated by using a radioactive source with a well-determined activity choosing the same image settings as used in patient scans as described in the paragraph 2.10.5..

$$\text{Activity}_{\text{VOI}} = \text{Total number of counts in VOI} \cdot \frac{1}{\text{Calibration Factor}} \qquad \text{Eq.2.10.4}$$

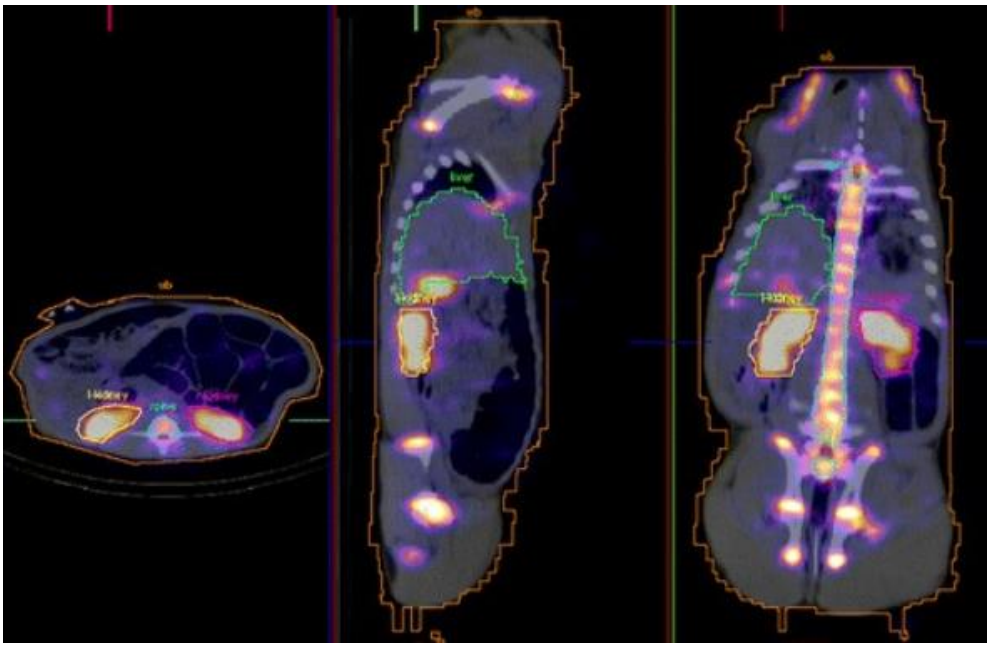

Figure 2.10.7: Axial, Sagittal and Coronal views of a SPECT/CT for ^{177}Lu injected Pig 1 (including drawn VOIs for selected organs)

However, due to partial volume effect (PVE), the counts in some small regions might be underestimated (*35*).

2.10.6. Biokinetics and Biodistribution Assessment (Sampling Time Points and Frequency)

The choices of sampling and scanning time points have a great impact not only on dosimetry but also on biokinetics and biodistribution (*38*). Early time points provide valuable information on the uptake pattern of the radiopharmaceutical biodistribution, whereas late time points are quite important for dosimetry assessments and have the greatest impact on the TIAC values which directly affect also the absorbed dose values (*6*). In order not to have under- or over-estimations in absorbed dose values and in order to have sufficient data leading to more accurate results for analyzing the biokinetics and dosimetry, both blood sampling and scanning time points must be selected based on the physical and chemical properties of used radionuclide and peptide analog.

2.10.7. Time-Integrated activity Coefficient (TIAC)

For dosimetry in nuclear medicine, the time integral over the fractional activity uptake in organs or lesions accumulating activity is required to calculate the time-integrated activity coefficients (TIACs) for the selected organs and the organs at risk. Since the calculated TIACs are used to calculate the absorbed dose values in the selected organs, the TIAC calculation has a great impact on the dosimetry. Even though having the optimal scan time(early/late follow up time points) and scan duration as well as optimal reconstruction parameters, unless the integration of time activity curves is accurate, either overestimations or underestimations in absorbed dose values can be observed as a result. Accurate and precisely TIAC calculation is challenging as it includes choosing a suitable set of fit function, finding optimal initial parameters for the fit, and as a last step computing the area under the curve with applying an adequate error model. All these issues and the proper implementation of the mathematical equations must be carefully analyzed while calculating TIACs. The area under the time-activity curve representing the TIAC can be calculated either by available software tools such as NUKFIT (*39*) or by applying manual fitting such as trapezoidal method, mono/biexponential fits (*31*). In contrast to NUKFIT, currently most of the available dosimetry software tools, despite having sophisticated image processing functionality or large data bases for S-values, have the disadvantage that they neither include methods for choosing the ideal fitting function, nor propagate the corresponding error calculation for the TIACs.

In NUKFIT, multiple fit functions can be selected and each fitting parameter can be modified by the user for the time activity curve of a selected organ. Then, the program lists the best fit options including their uncertainty which is estimated using the standard errors of the fitted parameters derived from the calculated variance-covariance matrix and Gaussian error propagation.

2.10.8. Absorbed Dose and Effective Dose Calculation

Absorbed Dose:

The quantity used to identify and measure the amount of radiation dose (Gy) received by any tissue or organ is the absorbed dose. Absorbed dose is the energy absorbed per unit mass of any material. The absorbed dose ($\overline{D}$) is defined as the mean energy imparted to target tissue per unit tissue mass (Eq.2.10.5a-b)(*32*). The time-independent factor S includes consideration of the types and energies of the radiations emitted, geometrical aspects such as the size and shape of the source and target regions, and the target-source distance and the composition of the absorbing and attenuating media (*31*).

$$\overline{D} = \tilde{A} \cdot S \qquad \text{Eq.2.10.5a}$$

$$\overline{\mathrm{D}} = \widetilde{\alpha} \cdot \mathrm{A}_0 \cdot \mathrm{S} \qquad \text{Eq.2.10.5b}$$

Where, $\tilde{A}$ (Bq·s): the time-integrated activity concentration, S value Gy/(Bq·s): the absorbed dose rate per unit activity, $\widetilde{\alpha}$: TIAC of the organ and A_0: administered activity.

There are specific software tools that are used for absorbed dose calculation such as MIRDOSE 3, OLINDA/EXM, NUKDOS, IDAC-DOSE, RADAR (*18,27,40,41*). The same patients' absorbed dose values may vary associated with the S values based on used phantom in the software tool. In the most common software tool OLINDA/EXM, standard phantoms representing the average patient (for organ doses) or a sphere model (for tumor doses) are used. Therefore, the resulting S values are not patient specific. For the deposited energy corresponding to the tumors and organs, the Monte-Carlo simulation based pre-calculated S values are used. To be more accurate and to account correction for alpha and beta emissions, the calculated absorbed doses must be adjusted with respect to the actual organ volumes. Then the absorbed doses scale linearly with the mass of the related organ.

As it is in OLINDA/EXM, IDAC-DOSE and RADAR, major restriction of the software tools using organ level dose estimation is assuming the uniform dose distribution in the certain organ which neglects the cross-dose to or from the tissues of corresponding organ.

Alternatively as it is in NUKDOS, absorbed doses can be also calculated by using the convolution of dose-point kernels. The dose-point kernel describes the distance-dependent energy deposition from a radioactive point source in a medium, which is dependent on the energy and yield of the emissions from the specific radionuclide (*42*). The radionuclide specific dose-point kernels convolved with the voxel activity distribution in the selected organ to generate dose rate for each voxel in the volume (*18*).

For more accurate dose estimation, there are Monte Carlo simulations that are able to take into account patient-specific source and target organ geometries and tissue inhomogeneities with considering non-uniform dose distribution. However, the usage of these codes may be quite complicated and time consuming due to long computation times, which make them unpractical for clinical use (*43*).

Effective Dose:

The quantity used for radiation protection is defined by the International Commission on Radiological Protection (ICRP) in publications 60 (*44*) and 103 (*45*) for establishing annual limits of exposure to workers and members of the general public and is named "effective dose" (unit: Sievert (Sv)) (*46*). The ICRP 60 report defines radiation weighting factors for better comparison of the biological effects of different particle types and tissue weighting factors for estimating the stochastic risk of cancer induction in organs. ICRP 103 updates the recommendations including the radiation and tissue weighting factors, based on the latest available scientific information of the biology and physics of radiation exposure. In the ICRP 103 recommendations, although there is no change on the operational quantities and dose limits, the updates on the radiation weighting factor (W_R) and the tissue weighting factor (W_T) independent of radiation type attributed the changes on the effective dose.

Organ	ICRP 60 W_T	ICRP 103 W_T
Gonads	0.20	0.08
Bone Marrow	0.12	0.12
Lung	0.12	0.12
Breast	0.05	0.12
Thyroid	0.05	0.04
Bone Surfaces	0.01	0.01
Remainder	0.05	0.12
Colon	0.12	0.12
Stomach	0.12	0.12
Bladder	0.05	0.04
Liver	0.02	0.04
Esophagus	0.02	0.04
Skin	0.01	0.01
Salivary Glands		0.01
Brain		0.01

Table 2.10.1: The Tissue Weighting Factors (W_T) in ICRP 60 and in ICRP 103 Publications (*45*)

The effective dose is the sum of the equivalent doses over a defined ensemble of organs and tissues each weighted by a tissue weighting factor (W_T). The radiation risk is modeled by W_T which reflects the radiosensitivity of tissues (*47*).

Equivalent dose is computed as the sum of absorbed doses ($\overline{D}$) in an organ or tissue (T) from all contributions by different types radiations multiplied by their respective radiation weighting factor (W_R) for radiation species (R) (*48*).

$$\text{Equivalent Dose} = H_T = \sum_R \mathrm{W_R} \cdot \overline{D} \qquad \text{Eq.2.10.6}$$

$$\text{Effective Dose} = \sum_\mathrm{T} \mathrm{W_T} \cdot \mathrm{H_T} \qquad \text{Eq.2.10.7}$$

3. Materials and Methods

3.1. Investigated Data and Analysis

The biodistribution, biokinetics and internal dosimetry of the ^{177}Lu labeled somatostatin receptor antagonist OPS201 (or JR11) used for therapeutic purposes) was investigated in preclinical (mice and pigs) and clinical studies. Five extrapolation methods were applied on blood, liver and kidneys of the animals to find an appropriate method, which minimizes the interspecies differences for biokinetics, in-vivo biodistribution and dosimetry. In addition to that, the biodistribution and internal dosimetry of the ^{68}Ga labeled somatostatin receptor antagonist OPS202 (or NODAGA-JR11) used for diagnostic purposes) were analyzed in clinical studies (^{68}Ga-OPS202 patients). Information related to the animals (mice and pigs) and patients included in this thesis can be seen in the following table 3.1.

OPS201 (SST2 antagonist - therapeutic agent)			
	Athymic Nude-Foxn1nu Mice	Danish-Landrace Pigs	Patients with Progressive NETs
Gender	28 Female	3 Female, 1 Male	3 Female, 2 Male
Weight	26 ± 1 g	28 ± 2 kg	61 ± 17 kg
Age	8 - 9 weeks	3 months	44 - 77 years
Radionuclide	^{177}Lu	^{177}Lu	^{177}Lu
Injected Activity	0.19 - 0.27 MBq	97 - 113 MBq	850 - 1086 MBq
Peptide Amount	0.017 µg	9 µg	55 - 106 µg

OPS202 (SST2 antagonist - diagnostic agent)	
	Patients with well differentiated G1/G2 GEP-NETs
Gender	5 Female, 7 Male
Weight	55 ± 19 kg
Age	32 - 74 years
Radionuclide	^{68}Ga
Injected Activity	125 - 189 MBq
Peptide Amount	15 µg

Table 3.1: Information about Species for OPS201 and OPS202 Labelled Preclinical and Clinical Studies

OPS201 raw data of mice were obtained in collaboration with the University Hospital of Basel, Switzerland (*3*) and of pigs' scans and blood samples were taken at Aalborg University Hospital, Denmark. The pig study was performed in close collaboration with the department of Nuclear Medicine in Würzburg and Octreopharm Sciences (*2*). OPS201 post-therapeutic human data were provided for analysis by Wild et al. (*4*)). For OPS202, the organ-specific activities of patients were obtained from PET scans carried out in a phase I study at the University Hospital Basel, Switzerland, in collaboration with Octreopharm Sciences. The dosimetry analysis was done in Würzburg and described in the publication by Nicolas et al.(*15*).

3.2. Imaging with OPS202 and OPS201 in Each Species

Pigs:

After injection of ^{177}Lu-OPS201, whole body (WB) planar images and SPECT/CT scans were acquired at multiple time points (0.5, 2, 3, 4, 50, 100, 150, 250h after administration) to quantify the organ uptakes. SPECT/CT data and WB planar images were acquired on a Siemens Symbia T16 ((Siemens Healthineers AG). The acquisition duration was 50 min for all scans: 10 min for planar WB imaging and 40 min for WB SPECT (2 bed positions of 20 min each). In addition, a low-dose CT was performed subsequent to SPECT imaging for attenuation correction. Reconstruction was performed with Flash3D (Siemens 3D OSEM with CT-based attenuation correction, triple energy window based scatter correction, and resolution recovery: 6 iterations and 6 subsets) (2).

Patients:

After injection of ^{177}Lu-OPS201, SPECT/CT data and WB planar images were generated with a BrightView XCT Philips SPECT/CT scanner equipped with medium-energy, parallel-hole collimators. WB scans and low-dose SPECT/CT were performed at 1, 3, 24, and 72 h after administration of 975 MBq mean activity of ^{177}Lu-OPS201 to analyze the selected organ uptakes. Attenuation and scatter correction were applied to the SPECT images (*4*).

After injection of ^{68}Ga-OPS202, WB PET/CT scans (dynamic: 0, 0.5 h and static: 1, 2 and 4 h) were acquired using the PET/CT scanner (Discovery^{TM} STE, GE Healthcare). A dynamic scan was conducted over the kidney region during the first 30 min; static scans were conducted from head to sub inguinal region at 0.5, 1, 2, and 4 h post-injection. A low-dose, non-enhanced CT scan was acquired using the following parameters: 120 keV, current modulation (smart 30-300 mA), 0.8s/rotation and pitch 1.75. All PET images were acquired at 4 min/bed position with 5-slice overlap. Attenuation corrected PET images were reconstructed iteratively (21 subsets, 2 iterations, 128×128 matrix for a 70-cm diameter of field-of-view), with standard pre-processing and post-processing filters (3 mm full width at half maximum) (13).

3.3. In-vivo biodistribution and biokinetics analyses with OPS202 and OPS201

^{177}Lu-OPS201:

To quantify the amount of activity, the percentage values corresponding to the injected radioactivity (A%) per organ as a function of time were calculated for the selected organs (See table 3.3) via a manual VOI analysis on multiple SPECT/CT scans (for pigs and patients) and via a gamma counter (for mice). For pigs, all VOIs were drawn based on the CT scan. To avoid spill-out effects, CT based organ VOIs were enlarged by 2 voxels in addition to their CT based volumes. For mice, sacrificed organs were counted by using well type gamma counter (3), the total numbers of count for the selected organs were reported and A% values were calculated. The time activity curves of blood for each species were analyzed separately from the collected samples. The population-based A% values of pigs were used to create the time activity curves for the selected organs and blood. The reason for this choice is that scan time points for each pig was not identical. In contrast, mean A% values could be used for the organs and median A% values for the blood in mice and humans since the same scanning and sampling times had been applied for all patients and mice.

To analyze the interspecies differences of the biokinetics of ^{177}Lu-OPS201, the time-dependent uptake data sets for the kidneys, liver and blood were used and separately fitted time-activity curves (TACs) including optimal fit function parameters were created for each species by using the software solution NUKFIT (*39*). The resulting fits and the time-dependent uptake data sets for the selected organs (Shown in table 3.3) were investigated to compare the biokinetics and biodistribution of OPS201 in the different species.

Selected Organs for The In-Vivo Biodistribution Analysis of ^{177}Lu-OPS201		
Mice	Pigs	Patients
Liver	Liver	Liver
Kidneys	Kidneys	Kidneys
Heart	Heart	*LV2-4
Lung	Bladder	Spleen
Pancreas	Spine	*WB
Spleen	Bone	
Femur	Remainder	
Remainder		

Table 3.3: Selected Organs for the In-Vivo Biodistribution Analysis of ^{177}Lu-OPS201

[*Lumbar Vertebra 2-4: (LV2-4), Whole Body: WB]

^{68}Ga-OPS202:

To quantify the amount of A% per organ as a function of time, several VOIs for selected organs of the patients (WB, pituitary gland, right parotid gland, heart, lung, liver, gall bladder, spleen, pancreas, adrenal glands, kidneys, urinary bladder, gastrointestinal-tract, LV2-4) were drawn based on each CT scan with avoiding spill-out effects. The WB uptake of the first scan was set to 100%. The time activity curves were generated for the blood and selected organs of the patients delineated on fused PET/CT images with taking into account renal excretion activity. Time activity curves for blood were analyzed separately from the collected samples.

3.4. TIAC Calculation in each ^{177}Lu-OPS201, ^{68}Ga-OPS202 Injected Species

For internal dosimetry, the TIACs of the selected organs and blood were calculated by integration of respective time activity curves for each organ and blood using the software solution NUKFIT (*39*), choosing the optimal fit functions as proposed by the code. The TIACs are estimated by analytically integrating the fitted functions. Their standard error values are determined assuming Gaussian error propagation. For this investigation, a systematic error of 10% in activity quantification was assumed for each measured data point. The TIAC of the urinary bladder content was integrated by using a trapezoidal integration method and assuming physical decay after the last data point. In addition to this, the TIAC of bone for the ^{177}Lu-OPS201 injected pigs was calculated based on the approach that 19% of the total skeleton mass is considered as the mass of the spine (*49*).

3.5. Blood and LV2-4 based Bone Marrow Dosimetry

In both diagnostic and therapeutic nuclear medicine, the determination of absorbed doses in the bone marrow is very important as the bone marrow is the critical organ for many therapies and most likely correlated with hematological toxicity. Due to the tissue composition, the activity distribution in bone marrow can be highly inhomogeneous and quantifying the activity concentration in bone marrow becomes a challenge. As there is no accepted optimal way for estimating the bone marrow absorbed dose, either blood based or image based techniques are generally used to calculate bone marrow absorbed dose (*50*).

^{177}Lu-OPS201: After administration of ^{177}Lu-OPS201, blood samples were taken up to 72 h for mice, up to 300 h for pigs, and up to 23 h for patients in order to measure the blood radioactivity contents by using the same well-type gamma counter. The patients' blood data were, originally, provided as relative values, normalized to the first blood sample immediately taken after injection. To convert the raw count values to blood uptake values per mL in each time point, patient blood data were quantified (in Bq/mL) retrospectively by using the same calibration factor as for the OPS201 mouse study. For all species, blood based absorbed doses for the red bone marrows were calculated according to the Shen method (*2,51,52*).In the blood based bone marrow dose calculation, with the consideration of no specific radiopharmaceutical binding in blood or red marrow, the time-integrated activity concentration in blood (C_{blood}) and the red marrow–to–blood activity concentration ratio (RMBLR) is used to calculate the time-integrated activity in the red marrow ($\widetilde{\mathrm{A}}_{\mathrm{RM}}$) defined as (*51,52*):

$$\widetilde{\mathrm{A}}_{\mathrm{RM}} = C_{\mathrm{blood}}/\rho \cdot \mathrm{RMBLR} \cdot \mathrm{m}_{\mathrm{RM}} \qquad \text{Eq. 3.5.1}$$

ρ: density, set to 1 g/cm^3, RMBLR: the red marrow–to–blood activity concentration ratio. RMBLR is set to 1 as, according to Forrer at al. (*53*), the activity in bone marrow aspirates correlates with the activity measured in blood for ^{177}Lu labelled [DOTA^0,Tyr^3]octreotate; m_{RM}: mass of the red marrow (m_{RM}= 1500g (*54*)).

$\widetilde{\mathrm{A}}_{\mathrm{RM}}$ is used as input for OLINDA/EXM to provide bone marrow absorbed doses (based on ICRP 60 weighting factors for a standard patient).

^{68}Ga-OPS202: Patient blood samples were taken at 2, 5, 10, 20, and 30 min, as well as at 1, 2, and 4 h after OPS202 injection. The image based red bone marrow absorbed doses were calculated according to the method described by Herrmann et al (*52*). In the image based method, 6.7% of the total bone marrow was assumed to be represented by Lumbar vertebra 2-4 (LV2-4). 1/0.067 times the calculated TIAC value of LV2-4 is used in OLINDA/EXM (*41*) to calculate the image based red bone marrow absorbed doses.

3.6. Using IDAC-Dose2.1 and NUKDOS for Voxel Based Dosimetry

For the OPS202 injected patients, by using the calculated TIACs of selected group of organs as input, the absorbed dose and effective dose coefficients for a 74 kg male patient were calculated using OLINDA/EXM (*41*) and IDAC-Dose 2.1 (*55*) (with applying the ICRP 60 weighting factors and CT based organ volumes). These calculated values were compared to published absorbed dose and effective dose coefficients of other alternative diagnostic agents (DOTATATE, DOTATOC and FDG) in the literature.

For the OPS201 injected pigs and patients, the absorbed dose coefficients of the selected organs were calculated by using the NUKDOS software solution (*18*) while for the OPS201 injected mice, the absorbed dose coefficients of kidneys were calculated using OLINDA/EXM (*41*) (using the spherical model).

3.7. Scaling In Preclinical Studies for Estimating Human Dosimetry

There are several extrapolation approaches that are used to estimate TIAC values, absorbed doses, in vivo biokinetics and biodistribution in humans based on animal data. Assuming the same biodistribution in animals and humans is the most common used method which means applying no extrapolation. In addition to this, relative mass scaling, time scaling, allometric scaling and the combined method of relative mass and time scaling are alternative techniques described in the literature. However, there is currently no common well-accepted method.

In this study, five interspecies extrapolation methods were applied on blood (only for the OPS201 injected pigs), kidneys and liver TIAC values (for mice and pigs) and examined to determine the optimal method for dosimetry (*13,14*). None of the extrapolation methods could be applied on blood TIAC values of mice since no data for the total animal blood volume was available.

Method 1 (eq. 3.7.1.) ("same bio-distribution approach"), is based on the assumption that the TIACs for the same organ in animals and humans are the same (*13*).

$$\mathrm{TIAC\ organ}_{\mathrm{human}} = \mathrm{TIAC\ organ}_{\mathrm{animal}} \qquad \text{Eq 3.7.1}$$

Method 2 (eq. 3.7.2.) is relative mass scaling in which the TIAC value in a human organ is set equal to the TIAC value in the same animal organ multiplied by the ratio of whole body and the selected organ mass of human and animal ($\left(\frac{\mathrm{m_{organ}}}{\mathrm{m_{WB}}}\right)_{\mathrm{human}}, \left(\frac{\mathrm{m_{organ}}}{\mathrm{m_{WB}}}\right)_{\mathrm{animal}}$) (*13*).

$$\mathrm{TIAC\ organ}_{\mathrm{human}} = \mathrm{TIAC\ organ}_{\mathrm{animal}} \times \frac{\left(\frac{\mathrm{m_{organ}}}{\mathrm{m_{WB}}}\right)_{\mathrm{human}}}{\left(\frac{\mathrm{m_{organ}}}{\mathrm{m_{WB}}}\right)_{\mathrm{animal}}} \qquad \text{Eq 3.7.2}$$

Method 3 (eq. 3.7.3.) is time scaling in which time (t) is scaled by a power function of the ratio of whole body masses of human and animal ($\mathrm{m_{WB_{human}}}, \mathrm{m_{WB_{animal}}}$) for calculating the TIACs. In Method 3, the exponent is set to 0.25 (*13*).

$$\mathrm{t\ organ}_{\mathrm{human}} = \mathrm{t\ organ}_{\mathrm{animal}} \times \left[\frac{\mathrm{m_{WB_{human}}}}{\mathrm{m_{WB_{animal}}}}\right]^{\frac{1}{4}} \qquad \text{Eq 3.7.3}$$

Method 4 is a combined method, first time scaling is applied (eq. 3.7.3), then the TIAC values of the animal are scaled based on relative mass scaling (eq. 3.7.2.) (*13*).

Method 5 (eq. 3.7.4.) applies allometric scaling in which TIACs of an animal are scaled by a power function of the ratio of WB masses of human and animal. The scaling component value was taken from the table 2 of the paper by Lindstedt S.L. et al. (*14*). In the paper, the scaling component value was predicted based on the anatomical parameters and biological rates of mammals such as heartrate, respiratory rate, cardiac output, ventilation and oxygen uptake rates. In method 5, the scaling component 'b' depends on the selected organ and is set equal to 0.92 for liver and 0.82 for kidneys (*14*).

$$\text{TIAC organ}_{\text{human}} = \text{TIAC organ}_{\text{animal}} \times \left[\frac{m_{WB_{human}}}{m_{WB_{animal}}}\right]^{[b-1]} \qquad \text{Eq 3.7.4}$$

Where: m: Mass, WB: Whole Body, b: Scaling Component, b(for liver)=0.92, b(for kidneys)=0.85.

3.8. 3D Printed Phantom Experiment

To find an adequate way of calculating absorbed dose values more accurately in ^{177}Lu labelled therapies, 2D and 3D quantitative imaging modalities were compared by using a 3D kidney printed phantom.

3.8.1 Preparation of 3D printed Phantom

A fillable one-compartment kidney phantom was designed and fabricated based on the right kidney volumes of ^{177}Lu-OPS201 injected pig 1(administered activity 107 MBq). The 3D printed kidney was modeled as an ellipsoid with semi-axes lengths taken from a VOI analysis of pigs performed in syngo.via (Siemens Healthineers AG). Here, the drawn kidney VOIs of a pig was rotated to coincide with the software coordinate system, and the dimensions were read out (See figure 3.8.1). The resulting semi-axis length, width and height were 9.73 cm, 5.10 cm, and 2.45 cm, leading to a nominal volume of 63 cm^3. The model was implemented as computer-aided design in Autodesk Inventor (Autodesk Inc). The design of the kidney phantom was exported in the stereolithography format and 3D-printed with a Form2 3D printer (Formlabs Inc). Then, the phantom was refined by washing in isopropyl alcohol, ultraviolet curing, removal of support material, thread cutting, and adding screws and o-rings (for filling and mounting).

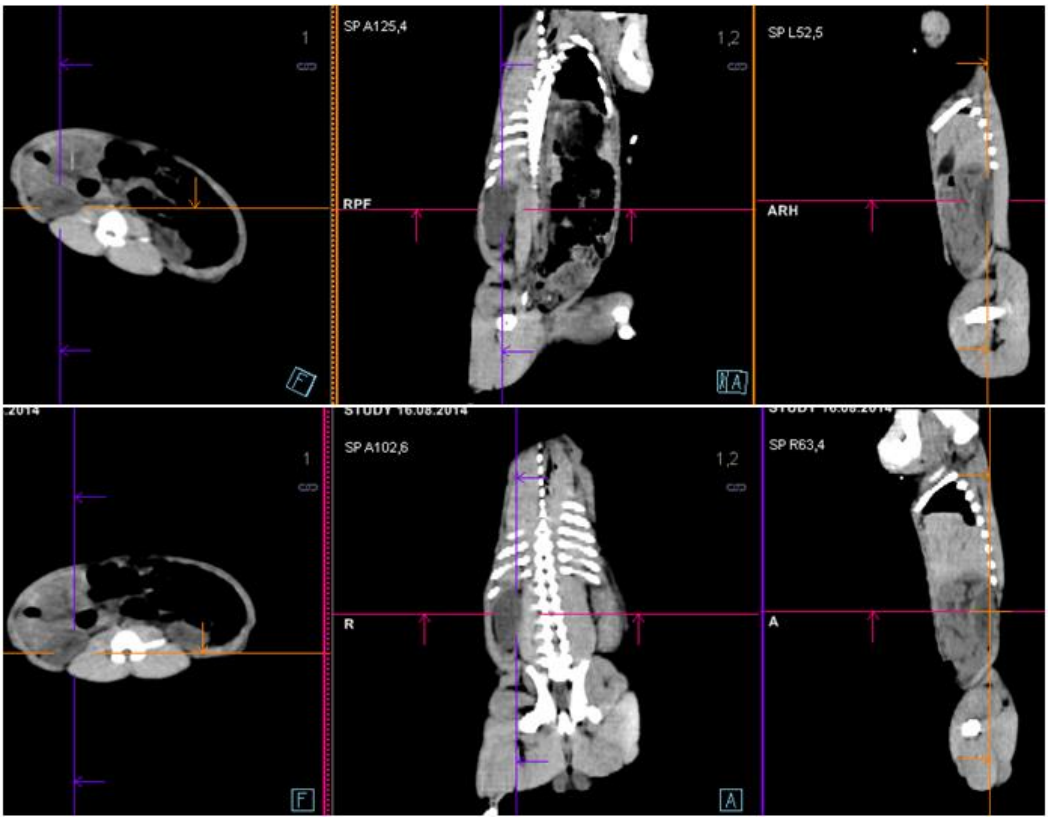

Figure 3.8.1: Dimensions of Ellipsoid, Axial, Coronal and Sagittal views of Pig 1 CT

[In the lower row of the figure the coordinate system of scanner was rotated in order to obtain the dimensions for the ellipsoid.]

3.8.2 Experimental Scans

The 3D printed kidney phantom was placed in the NEMA NU2-2001 PET/SPECT-Phantom (figure 3.8.2).

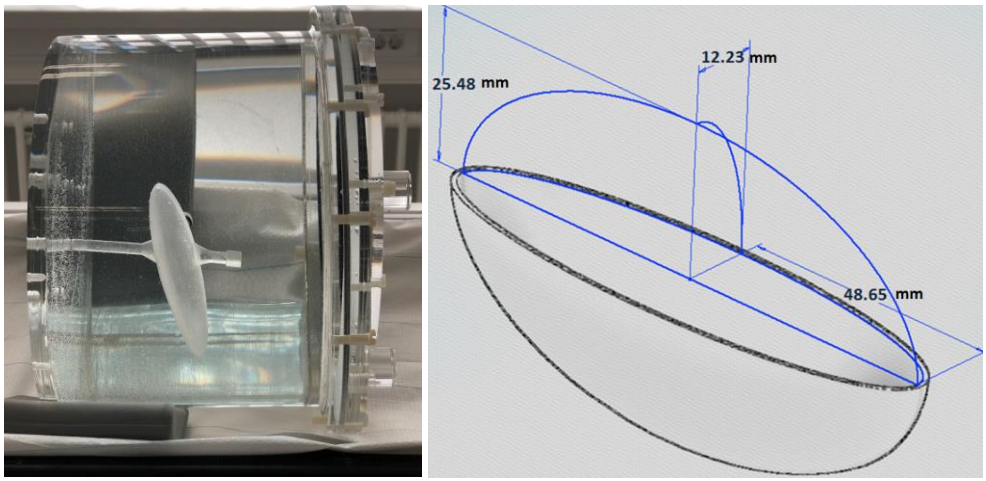

Figure 3.8.2: The NEMA NU2-2001 PET/SPECT-Phantom Including 3D Printed Kidney Phantom

[At the right hand side of the figure, the semi-axis length, width and height of the 3D printed kidney compartment: 9.73 cm, 5.10 cm, and 2.45 cm, leading to a nominal volume of 63 cm^3 are shown]

The phantom including the 3D printed kidney phantom filled with 3.65 MBq ^{177}Lu was scanned with and without background activity (total activity in the phantom with background activity: 49.6 MBq). After the scans, 3 sets of aliquots from each the 3D printed kidney compartment and the background were taken and measured in a high purity germanium detector. The mean values of the measured total number of counts for the aliquots, taking into account the ^{177}Lu decay were used to calculate the exact amount of activities in the printed kidney compartment and the background of the phantom. The activity concentration for kidney phantom and the background was 57.1 ± 0.75 kBq/ml and 5.72 ± 0.11 kBq/ml respectively. The activity concentration ratio between the background and the kidney compartment of the phantom was 9.94.

In order to simulate the same biodistribution, instead of repeating 2D and 3D measurements at multiple time points, acquisition time of SPECT/CT and planar scans were adjusted to have the same count rate as it was for all time points of the ^{177}Lu-OPS201 injected pig 1 SPECT/CT scans. With this practical way all scans were completed in one day. Identical reconstruction settings and acquisition parameters (except acquisition time) as used for ^{177}Lu-OPS201 injected pigs scans were applied for the phantom.

Based on the multiple SPECT/CT images of pig 1, the highest A% within the first day was calculated at 3 h. To investigate the spill-in, spill-out effect and background-count influence on the TIAC, the kidney A% of the phantom with/without background on 3h planar and SPEC/CT images were adjusted corresponding to the 3h A% value of pig 1 SPECT/CT scan (activity of the pig 1 kidney at 3 h based on multiple SPECT/CT: 2.5 MBq).

Additionally, to optimize a technique for kidney absorbed dose calculation, TIAC values for the phantom with/without background activity were calculated by using multiple planar images with one SPECT/CT (MP1S imaging) and also by using multiple SPECT/CT images. For both imaging methods, NUKDOS is used for the calculation of the TIACs. The MP1S imaging method contains multiple planar scans and one SPECT/CT scan (at the identical time point of the 3 h planar scan). In order to calculate TIACs by using MP1S imaging, the 3 h SPECT/CT is used to scale the calculated percentage activities of drawn ROIs on planar images. Furthermore, the difference on calculated TIACs and TIAC errors by using NUKDOS was investigated by eliminating the late two time points to show the effect of late time points on dosimetry and absorbed dose values. The TIAC error values were determined by NUKDOS assuming a Gaussian error of 10% for each data point. All calculated TIACs and fit parameters were compared with pig 1.

4. Results

4.1. Dosimetry in Patients with OPS202 Used for Diagnostic Purposes

As a result of integrating the time activity curves of the selected organs for the OPS202 injected patients using NUKFIT with choosing optimal fit function, the absorbed dose coefficients and effective dose values were calculated by using OLINDA/EXM and IDAC-Dose 2.1. Kidney time activity curves of each patients and mean TIACs can be seen in figure 4.1 and table 4.1.1 respectively. Mean absorbed dose coefficients and effective dose values can be seen in the table 4.1.1. TIACs of the selected organs listed in appendix table 9.1.

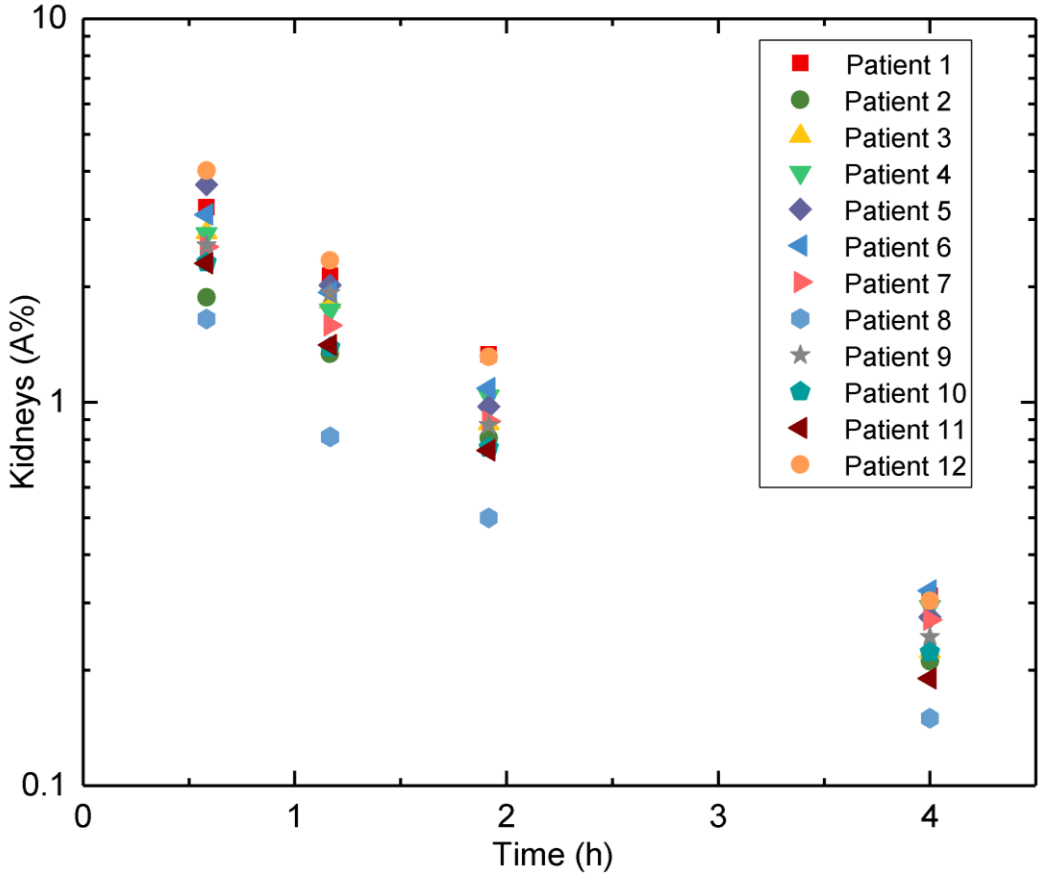

Figure 4.1: Percentage Activity (A%) of the Kidney versus Time for OPS202 Injected Patients

Organs	Mean TIAC	Standard Deviation	Units
Whole Body	1.337	0.073	h
Remainder	0.944	0.101	h
Liver	0.072	0.020	h
Kidneys	0.057	0.014	h
Heart	0.012	0.004	h
Adrenal glands	0.001	0.000	h
Gallbladder	0.001	0.000	h
Lower Large Intestine	0.018	0.003	h
Upper Large Intestine	0.018	0.003	h
Small Intestine	0.018	0.003	h
Stomach	0.018	0.003	h
Lung	0.044	0.010	h
Pancreas	0.002	0.001	h
Spleen	0.027	0.017	h
LV2-4	0.002	0.001	h
Blood	0.040	0.018	h
Red Bone Marrow	0.027	0.009	h
Urinary Bladder	0.086	0.030	h

Table 4.1.1: Calculated Mean Organ TIACs and Standard Deviations for OPS202 Injected Patients

Organs with high consistent absorbed doses are the urinary bladder (0.1E-01 mGy/MBq) and kidneys (8.43E-01 mGy/MBq). The calculated mean absorbed dose coefficients and effective dose values based on OLINDA/EXM (*41*) and IDAC-Dose 2.1 (*55*) were identical (only for ICRP60 coefficients).

Organs	Mean Absorbed Dose Coefficient (mGy/MBq)	Standard Deviation
Adrenals	2.99E-02	1.16E-02
Brain	7.32E-03	1.72E-03
Breasts	7.45E-03	1.70E-03
Gallbladder Wall	1.22E-02	3.10E-03
LLI Wall	3.54E-02	1.03E-02
Small Intestine	1.89E-02	4.50E-03
Stomach Wall	2.30E-02	7.53E-03
ULI Wall	2.60E-02	6.98E-03
Heart Wall	1.47E-02	3.83E-03
Kidneys	8.43E-02	3.13E-02
Liver	2.18E-02	8.66E-03
Lungs	2.12E-02	7.01E-03
Muscle	8.50E-03	1.68E-03
Ovaries	1.10E-02	1.68E-03
Pancreas	1.55E-02	5.09E-03
Red Marrow	1.13E-02	3.08E-03
Osteogenic Cells	1.39E-02	3.55E-03
Skin	7.13E-03	1.69E-03
Spleen	6.02E-02	4.73E-02
Testes	8.52E-03	1.70E-03
Thymus	8.41E-03	1.73E-03
Thyroid	8.04E-03	1.73E-03
Urinary Bladder Wall	1.01E-01	4.28E-02
Uterus	1.19E-02	1.72E-03
Mean Effective Dose Coefficient (mSv/MBq) : 2.40E-02		1.78E-03

Table 4.1.1: Calculated Mean Absorbed Dose Values and Effective Dose Coefficient for OPS202 Injected Patients (Including Standard Deviations)

The calculated mean effective dose coefficient of patients was 2.4E−02 ± 0.2E−02 mSv/MBq, which results in 3.6 mSv for a 150 MBq injection of ^{68}Ga-OPS202. This value is similar to those of other ^{68}Ga labelled compounds (*17,56-58*) (see in table 4.1.2.).

	DOTATATE Sandstrom (*57*)	**DOTATOC Hartmann (*56*)**	**DOTATOC Sandstrom (*57*)**	**FDG ICRP106 (*58*)**	**DOTA-JR11 Krebs (*17*)**	**OPS202 This Work**
Effective Dose coefficient (mSv/MBq)	0.021	0.023	0.021	0.019	0.022	0.024
Typical Injected Activity (MBq)	185	185	185	370	150	150
Effective Dose (mSv)	3.9	4.3	3.9	7.0	3.3	3.6

Table 4.1.2: Effective Dose Values for ^{68}Ga Labelled Compounds
[Typical injected activity information was based on (*59*).]

4.2. Dosimetry in Each Species with OPS201 Used for Therapeutic Purposes

The respective species-dependent time activity curves based on the drawn VOIs and well-type gamma counter analysis for the kidneys, liver, and blood are displayed in figures 4.2.1-3. Symbols represent time-dependent percentage uptake data sets for the selected organs and blood, while lines represent separated fits including fit function parameters from NUKFIT for the selected organs and blood in each species. Kidneys, liver, or blood fit curves including fit functions were named using the first letter of the selected organs (**K**idneys, **L**iver, **B**lood) and the species (**M**ice, **P**igs, **H**umans), resulting in the nomenclature KM, LM, or BM for mice, KP, LP, or BP for pigs, and KH, LH, or BH for humans. Since a logarithmic scale was used in all figures for better visualization, the error bars cannot be displayed completely. All standard deviation values determined assuming Gaussian error propagation were less than 10% (shown in appendix table 9.2). The calculated λ values used to create separated fits for the time activity curves by using the optimal fit function parameters from NUKFIT for each species and their organs are shown in appendix table 9.2. The shapes of kidney curves for each species were similar (figure 4.2.1).

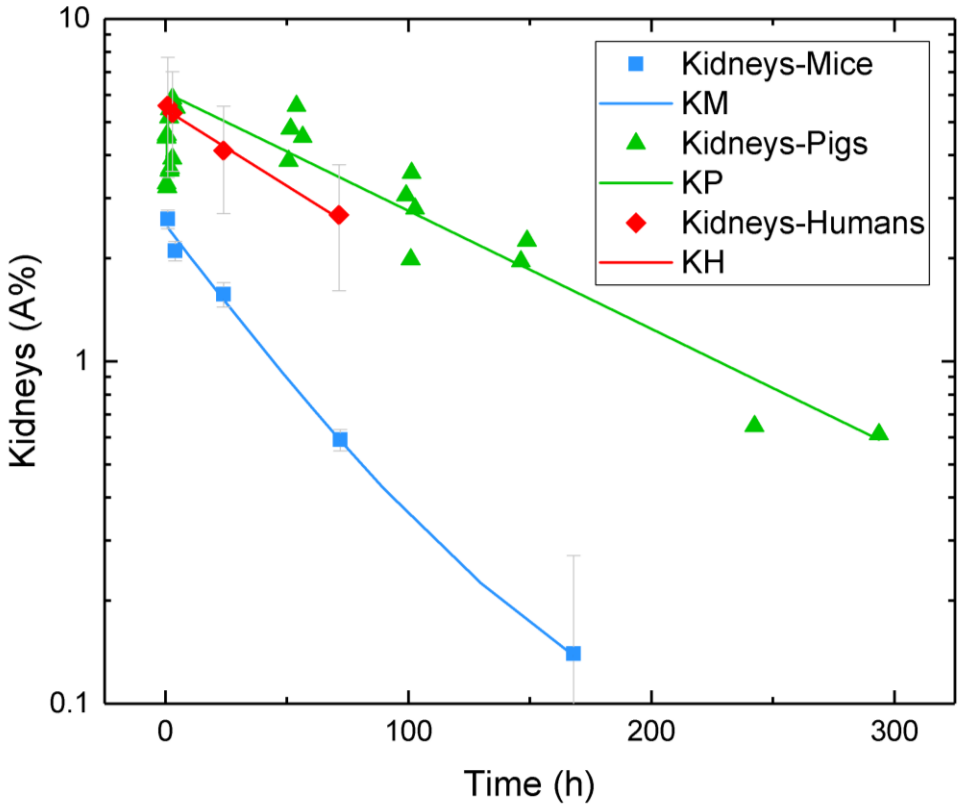

Figure 4.2.1: Time Activity Curves of the Kidneys Based on VOI and Well-Type Gamma Counter Analysis for Each Species

[Symbols: time-dependent percentage uptake data sets for the kidneys, Line: fit curves for the kidneys including fit function parameters from NUKFIT for mice (KM), pigs (KP), and humans (KH), respectively. All standard deviation values were less than 10% (see appendix tables 9.3.a and b).(*6*)]

The best approximation for the last phase (>50h) of the liver curves for all species was a mono-exponential function. The slope of the last phase was lower than the corresponding function of the pigs and the humans. In comparison to the patients, pigs show higher liver retention (figure 4.2.2).In addition, mice have slower decay rate than patients and pigs for the last phase (>50h) of the liver curve (figure 4.2.2).

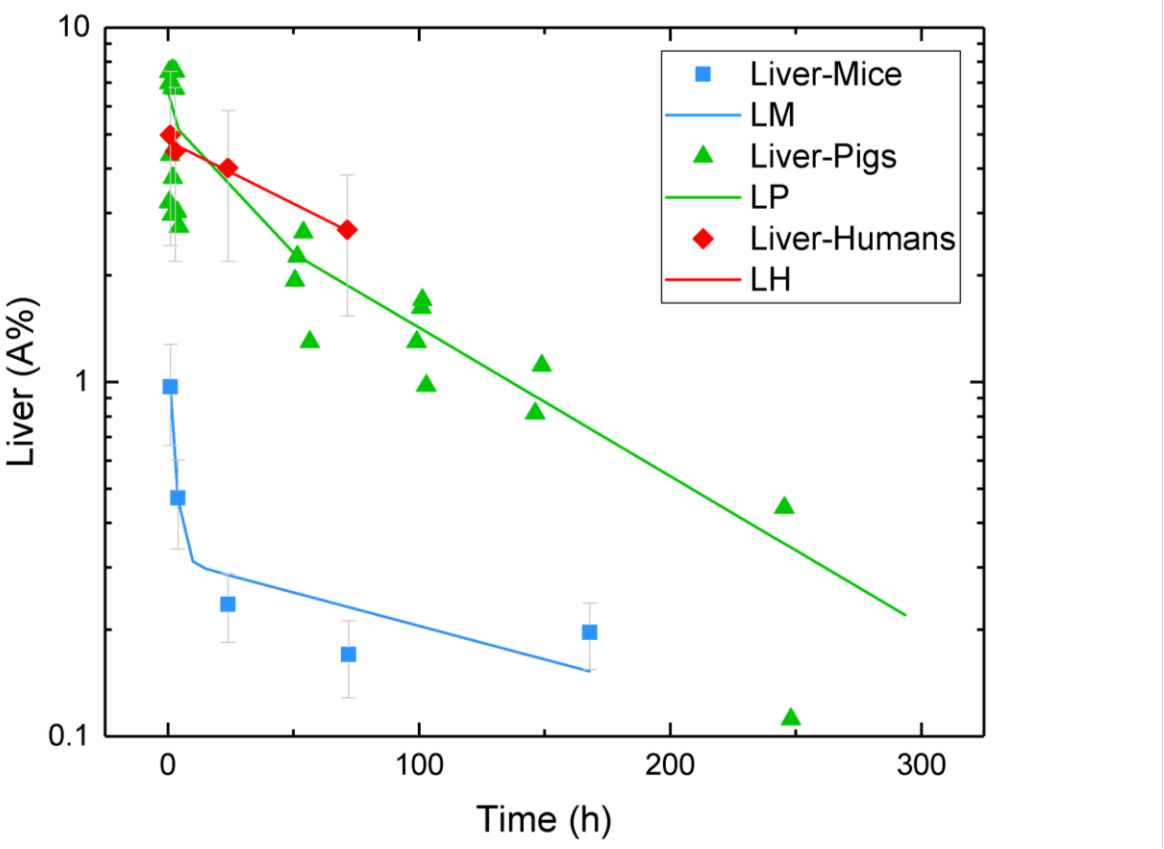

Figure 4.2.2: Time Activity Curves of the Liver Based on VOI and Well-Type Gamma Counter Analysis for Each Species

[Symbols: time-dependent percentage uptake data sets for the liver. Line: fit curves for the liver including fit function parameters from NUKFIT for mice (LM), pigs (LP), and humans (LH), respectively. All standard deviation values were less than 10% (see appendix tables 9.3.a and b)(*6*)]

A fast blood clearance of the compound is observed in the first phase (largest half-life: 1.83 h, see appendix tables 9.3.a-b) for each species. 10 min after injection, less than 5% of the injected activity per milliliter of blood circulates in pigs and humans (figure 4.2.3). Overall, the blood clearance of OPS201 in pigs and humans was faster compared to mice.

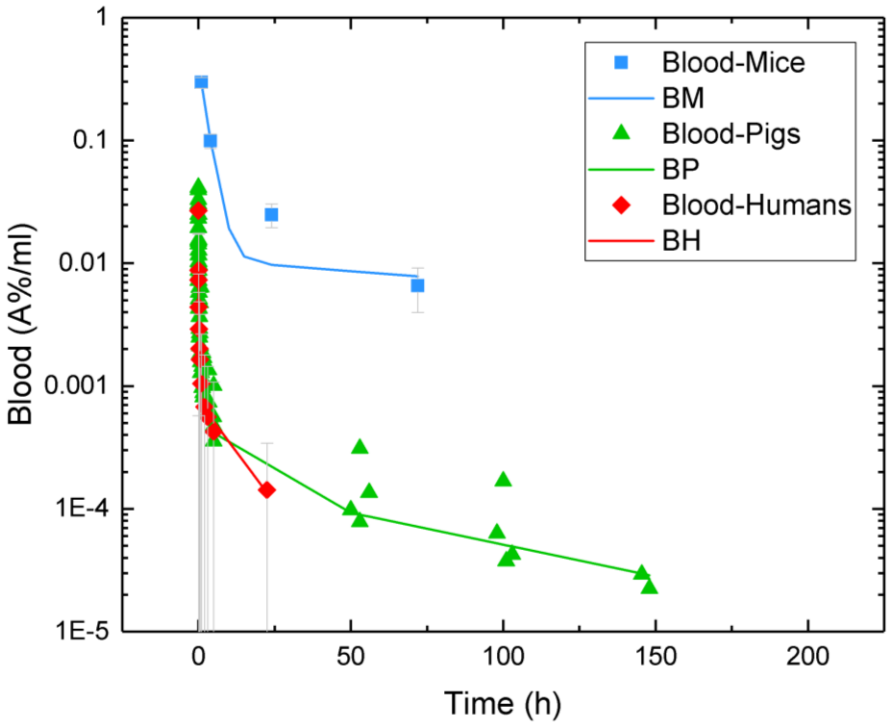

Figure 4.2.3: Time Activity Curves of Blood Based on Well-Type Gamma Counter Analysis for Each Species

[Symbols: time-dependent percentage uptake data sets for the blood. Line: fit curves for the blood including fit function parameters from NUKFIT for mice (BM), pigs (BP), and humans (BH), respectively. All standard deviation values were less than 10% (see appendix tables 9.3.a and b) (*6*).]

The resulting TIACs of species and the calculated TIACs of mice and pigs based on extrapolation methods are summarized in the tables 4.2.1-2. The kidney TIAC values were 1.44 h, 7.67 h and 5.85 h for mice, pigs and patients respectively.

	Kidneys TIAC ± Error (h)	Liver TIAC ± Error (h)	Blood TIAC ± Error (h/ml)
Mice	1.44 ± 8.5E-02	0.75 ± 4.1E-02	0.0370 ± 2.0E-03
Pigs	7.67 ± 1.8E-01	4.08 ± 9.4E-02	0.0002 ± 3.4E-06
Humans	5.85 ± 4.2E-01	5.32 ± 3.4E-01	0.0002 ± 8.2E-05

Table 4.2.1: Time-Integrated Activity Coefficients (TIAC (unit: h)) of the Selected Organs for each species with Respective Error Values Calculated by NUKFIT with An Assumption of 10% Systematic Error

	Kidneys TIAC (h)		Liver TIAC (h)		Blood TIAC (h/ml)
	Mice	Pigs	Mice	Pigs	Pigs
METHOD 1	1.44	7.67	0.75	4.08	0.00020
METHOD 2	0.43	4.17	0.32	1.04	0.00022
METHOD 3	3.89	8.73	0.88	4.65	0.00025
METHOD 4	1.17	4.75	0.38	1.18	0.00026
METHOD 5	0.44	6.63	0.40	3.78	0.00021

Table 4.2.2: Time-Integrated Activity Coefficients (TIAC (unit: h)) for the Selected Organs of the Animals Based On The Different Scaling Methods To Estimate Human TIAC Using Either Mice Or Pig Data Set As A Reference

Applying method 1 (“same biodistribution approach”) to the mice data for both kidneys and liver resulted in an underestimation by a factor of 4 for the kidneys and a factor of 7 for the liver compared to the patient data (kidney TIAC: mice=1.4 h and patients=5.9 h; liver TIAC: mice=0.7 h and patients=5.3 h). On the contrary, since pigs mimic the human metabolism better than mice. Method 1 in pigs results in a slight overestimation for the kidneys and a slight underestimation for the liver by a factor of 1.3 (table 4.2.1). The best agreement in TIAC was obtained by applying method 3 (“time scaling”) and method 4 (“combined relative mass and time scaling”) (see table 4.2.2). The other applied methods resulted in higher deviations. The kidney TIAC values of mice (except the results after applying method 3) are underestimated by a factor of approximately 4 in methods 1 and 4, and overestimated by a factor of 12 by applying methods 2 (“relative mass scaling”) and 5 (“allometric method”).

In contrast to the mice data, the kidney TIAC values of the pigs showed smaller variations; the data are overestimated by factors between 1.2 and 1.6 in methods 1, 3, and 5. For the mice liver, the TIACs, despite the scaling (even with applying method 3), were underestimated approximately by a factor of 6 (in method 3) up to 17 (in other methods). For the pig liver, TIAC values, underestimations approximately by a factor of 5 only in method 2 and method 4 were calculated, while all other applied methods showed similar results.

The mean absorbed dose values for a human using method 1 would be 0.08 Gy/GBq (based on mice), 2.30 Gy/GBq (based on pigs) compared to the absorbed dose calculated with human biokinetics data: 1.70 Gy/GBq. For humans after an injection of 5 GBq ^{177}Lu-OPS201, the highest absorbed doses were obtained for the kidneys (13.7 Gy), the osteogenic cells (3.9 Gy), the urinary bladder wall (1.8 Gy), and the liver (1.0 Gy). As for the bone marrow absorbed dose estimations, the calculated blood based bone marrow absorbed dose values are well below the critical organ dose limits (<2 Gy) (*60*).

4.3. Results Based on the Measurements of the 3D Printed Kidney Phantom

The resulting time activity curves for the phantom with/without background activity and pig 1 based on MP1S and multiple SPECT/CT imaging are shown in figure 4.3.1. Based on the created time activity curves (see figure 4.3.1) for the 3D printed phantom and pig 1, the highest A% values based on multiple SPECT/CT-based images were calculated for the first phase of the curves (< 54 h). As expected and planned, the same tendency of increase (< 54 h) and decrease (after 54 h) in A% values were obtained for the phantom and pig 1. The same tendency was observed for the A% values obtained by using MP1S for the 3D printed phantom. In contrast, there is no increase in A% for the MP1S-based analysis of pig 1. Instead, the highest A% value is reached for the first time point of the planar scans in that case (0.65 h).

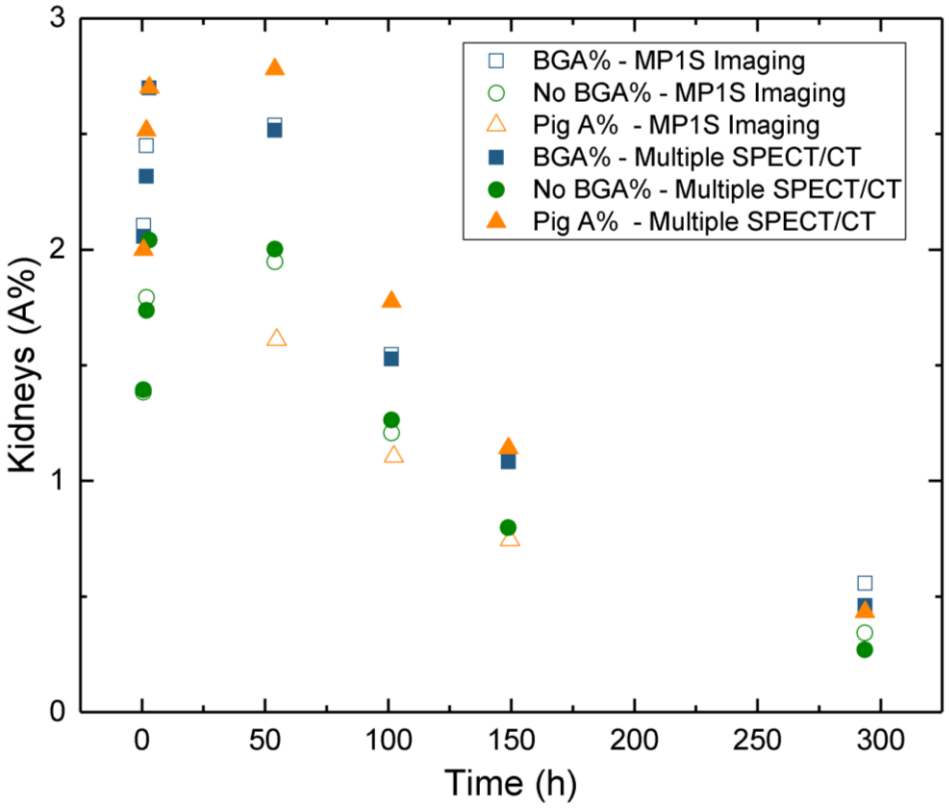

Figure 4.3.1: Time Activity Curves for the Kidney Phantom with/without Background Activity and Pig 1 Based on Multiple SPECT/CT and MP1S Imaging

[BGA% represents the kidney percentage activity of the phantom with background activity, no BGA% represents the percentage activity of the kidney in the phantom without background activity, pig A% represents the percentage activity of the right kidney in pig 1. MP1S imaging represents the combination of multiple planar images with one SPECT/CT (at identical time point of 3h planar image). In order to simulate the same biodistribution, acquisition duration time of SPECT/CT and planar scans of kidney phantom were adjusted to have the same count rate as it was for all time points of the ^{177}Lu-OPS201 injected pig 1 SPECT/CT scans.]

MP1S and multiple SPECT/CT based TIACs including all time points and excluding late two time points were calculated for Pig 1 and the 3D printed kidney phantom (with/without background). Calculated TIAC values are shown in the table 4.3 and figure 4.3.2.

Used Time Points and Imaging Modalities	Phantom NOBG TIACs (h)	Phantom BG TIACs (h)	Pig 1 TIACs (h)
all TP - MP1S	3.45	4.91	3.28
all TP - Multiple SPECT/CT	3.24	4.46	4.68
last TP eliminated - MP1S Imaging	3.58	4.93	3.20
last TP eliminated - Multiple SPECT/CT	3.55	4.97	5.11
last 2 TP eliminated - MP1S Imaging	4.84	6.24	2.95
last 2 TP eliminated - Multiple SPECT/CT	5.00	6.18	6.96

Table 4.3: The Calculated TIACs by Using Multiple SPECT/CT and MP1S Imaging for the Phantom and Pig 1 Based on Using Different Sets of Time Points

[Phantom NOBG and Phantom BG represent the 3D printed kidney phantom without and with background activity respectively. TP: time point. MP1S Imaging represents multiple planar scans in combination of one SPECT/CT image]

The TIAC investigations based on MP1S imaging (including all time points) for the 3D printed phantom showed a higher TIAC for the phantom with background activity (by factor of 1.42) compared to the TIAC for the phantom without background activity.

For the MP1S-based TIAC comparison (including all time points), the TIAC of the 3D printed kidney phantom with and without background activity was 1.50 and 1.05 times higher than pig 1, respectively. On the other hand, the multiple SPECT/CT based TIACs (including all time points) for the phantom with and without background activity were 1.04 and 1.44 times lower than for Pig 1, respectively.

When the TIACs (including all time points) based on MP1S imaging for the phantom with/without background activity are compared to the pig 1 TIAC based on multiple SPECT/CT, the calculated TIAC for the phantom containing background activity was higher by a factor of 1.05 in comparison to the multiple SPECT/CT based pig 1 TIAC. In contrast, the TIAC for the phantom without background activity was lower by a factor of 1.36 in comparison to the pig 1 TIAC based on multiple SPECT/CTs.

In addition to the comparisons between the kidney phantom and pig 1, the calculated pig 1 TIACs based on multiple SPECT/CTs and MP1S imaging were investigated separately. The multiple SPECT/CT based TIAC (using all time points) for pig 1 was higher by a factor of 1.4 in comparison to the MP1S based pig 1 TIAC. Without the late time points, this factor rose by a factor of 2.4 (see table 4.3).

Without the late time points for the multiple SPECT/CT based analysis, up to 1.5 times higher TIAC values were observed. The same tendency was also seen for the MP1S based analysis of the phantom. However, eliminating late time points from the MP1S based time activity curve of pig 1 results in lower TIAC by a factor of 1.1. The effect of eliminating the late time points on TIAC uncertainty values was seen as an increase up to by a factor of 4.4 for the phantom with/without background and the pig 1 TIAC errors obtained by using both imaging modalities. This effect can be seen in the figure 4.3.2.

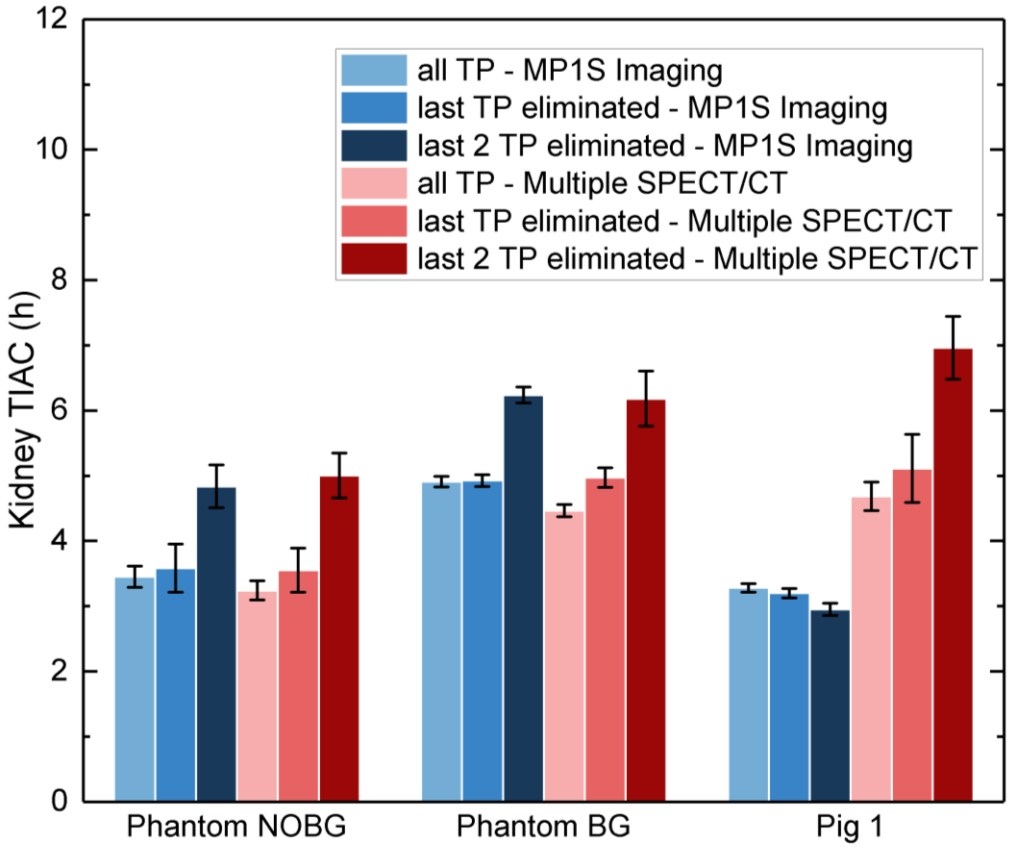

Figure 4.3.2: The Difference on Kidney TIACs with corresponding NUKDOS error values, in the Phantom with/without Background Activity and Pig 1 Calculated by Using NUKDOS with Eliminating the either the last or the last two Time Points

[TP: Time points, MP1S: Multiple planar images with one SPECT/CT image, Phantom NOBG: Phantom without Background Activity, Phantom BG: the Phantom with Background Activity]

5. Discussion

In vivo biokinetics and biodistribution of ^{177}Lu-OPS201 and ^{68}Ga-OPS202 for selected organs in different species (mice, pigs, and humans) with the dosimetry analysis on liver, kidneys, and bone marrow were investigated by using well-type gamma counter measurements, multiple WB planar and SPECT/CT images.

OPS202 is rapidly cleared from the blood, resulting in low background activity, especially in the liver and gastrointestinal tract with expressing high tumor contrast. The observed low background activity contributes to the tumor detection in organs that are potential sites of primary or metastatic disease. In addition, based on the investigations on OPS202 in patients, the optimal imaging time was evaluated as between 1 and 2 h to have high image contrast and high number of lesions' detection. The effective dose is similar to the other ^{68}Ga-labeled somatostatin receptor analogs. The calculated mean effective dose coefficients for the ^{68}Ga-OPS202 injected patients (0.024 mSv/MBq) were similar to the other ^{68}Ga labelled clinical studies with SSTR analogs in the literature (^{68}Ga-DOTATATE: 0.026 and 0.021 mSv/MBq (*57,59*), ^{68}Ga-DOTATOC 0.021 and 0.023 mSv/MBq (*56,57*), ^{68}Ga-DOTANOC: 0.025 mSv/MBq (*61*), ^{68}Ga-DOTA-R11:0.022 mSv/MBq (*17*)). The organs with the highest absorbed dose coefficients were the urinary bladder wall and kidneys. Despite the similar effective doses compare to other ^{68}Ga labelled compound, there were differences in the biodistribution among these tracers resulting in different organ doses. The most pronounced differences were for the liver, lung, and spleen. For instance, calculated liver absorbed dose values for ^{68}Ga-OPS202 patients were lower compared to the studies with ^{68}Ga-DOTATOC in the literature. The potential reason is clinically relevant since OPS202 exhibits substantially higher tumor-to-background ratios and sensitivity for detecting liver metastases (*16*).

With regard to the created time activity curves of blood for each OPS201 injected species, in the first phase, the observed fast blood clearance of OPS201 (<56 h) was in agreement with studies of the agonist (*62,63*). Sandstrom et al. (*63*) observed a first phase with a mean effective half-life of 1.6 h, in agreement with our OPS201 mice (1.8 h) and pigs (1.7 h) data. For humans, most likely because of the short observation period, the value was lower (0.5 h). For the late phase in pigs, our result (58 h) is also close to the results obtained in the human study with the agonist (43 h). Part of an ongoing phase 1 study with ^{177}Lu-OPS201 in patients with SSTR-positive progressive NETs by Nicolas et al. (*64*), in which dosimetry data are taken also at time points later than 48 h, is to substantiate whether the biokinetics of the agonist and antagonist in the pig model are comparable to those in the patients after ^{177}Lu-OPS201 treatment.

The calculated mean absorbed dose values of the kidneys for the OPS201 injected patients was 1.70 Gy/GBq. As a result of a 5 GBq ^{177}Lu-OPS201 administration to patients, the mean kidney absorbed doses were calculated to 8.5 Gy, which means that at least two times 5 GBq ^{177}Lu-OPS201 can be safely administered to the patients without reaching the critical organ dose for the kidney (23 Gy). After the second cycle of the treatment, in order not to have kidney toxicity patient specific dosimetry should be performed to determine the amount of injected activity for further cycles.

In comparison to OPS201 injected patients, visible spine and bone uptake and lack of spleen uptake was observed on animal scans. In addition, based on the time activity curves for OPS201, pigs show higher liver retention in comparison to patients. All observed interspecies differences, based on organ activity measurement either in a well counter or by scans and the subsequently fitted time activity curves (for kidneys, liver and blood), which are used to investigate the biokinetics, show the necessity of scaling. Five published scaling methods in the literature were tested on the kidneys and liver of OPS201 injected mice and pigs as well as on the blood data of OPS 201 injected pigs in order to identify an appropriate extrapolation method which minimizes the interspecies differences for comparing biokinetics, in vivo biodistribution, and dosimetry. All the applied extrapolation methods except time scaling (Method 3) result in a weight-dependent decrease of TIAC values and, consequently, the absorbed doses. For high organ-mass ratios between any two species (e.g., for mice compared to humans), to predict in vivo biokinetics, dosimetry, and absorbed doses in humans based on animal data more accurately, either time scaling (Method 3) or combined relative mass and time scaling (Method 4) should be applied instead of commonly used same biodistribution approach (Method 1, see chapter 3.7).

Not only scaling but also the follow-up period after injection plays an important role when investigating the biokinetics of therapeutic/diagnostic agents. The data at early time points, after the injection time, provide valuable information of the uptake pattern of the radiopharmaceutical. As well as the data at early time points, the late time points are quite important for biodistribution and dosimetry assessments since they have the greatest impact on the TIAC values that, as a consequence, directly affect also the absorbed dose values. In our study, the follow-up time in mice and patients was rather short for the biokinetics and dosimetry analysis of ^{177}Lu-OPS201. The blood samples were taken from 1 h up to 72 h for OPS201 injected mice and from 0.3 h up to 23 h for OPS201 injected patients. We are missing the early phase (for mice) and late phase (for mice and humans) of the biokinetics. Additional data on both early and late (at least up to 150 or 200 h) scan time points including blood sampling are required for more accurate analysis of the biokinetics and dosimetry, despite the fact that the decay patterns in each species were similar.

Since the follow-up time of blood in mice and humans was not sufficient and, additionally, because of high variability in the median values for humans and mice blood data, mice blood data were excluded from the extrapolation method analyses. In addition, there is a lack of information about the total blood volume of mice; thus, the uptake of the radiopharmaceutical cannot be deduced. Since we do not have these limitations in pigs, five extrapolation methods were applied on the pig blood data set. Besides, in pigs, measurements could be carried out over a longer period for dosimetry, biokinetics, and biodistribution assessments of therapeutic agents as compared to rodents, which makes the analyses more stable and accurate.

Mouse models are widely applied in cancer translational researches. On the contrary, in small animals like mice, despite the applied extrapolation methods, interspecies differences may still be observed. For instance, in our study, none of the applied extrapolation methods on mice liver TIAC values provided similar values compared to humans due to the biphasic clearance of the OPS201 agent from the mice liver which was different compared to pigs and humans. These results show the necessity to investigate the other physiological parameters such as organ size, heartbeat rate, and, as a consequence, faster biological half-life of radioactive compounds in the mice (*65*). In addition, gender-specific differences may play a role that is why the setup of the studies needs to be optimized also to address these potential effects.

As kidneys are one of the organs at risk in ^{177}Lu labelled treatments, an investigation of the influence of image quantification by using 3D scans versus a combination of 2D/3D imaging was performed by using a 3D printed phantom corresponding to multiple 3D pig 1 scans. For that purpose, dosimetry data based on multiple SPECT/CT and multiple planar images in combination with one SPECT/CT image was compared.

The consistency of calculated A% values in each SPECT/CT and planar scan of the phantom (which were chosen to mimic the multiple SPECT/CT based A% values of pig 1) showed that the chosen count rates and activities represent well the actual pig 1 data set.

On the other hand, because of the different count homogeneity in the background region coming from nearby areas in the phantom and in pig 1 resulted in a 1.5-fold difference between MP1S imaging based TIACs of the phantom with background activity and pig 1. In addition, due to spill-in effect, the MP1S imaging based TIAC of the phantom without background activity was higher than the phantom with background activity.

As for the multiple SPECT/CT based TIAC comparison between the phantom without background activity and pig 1, the 1.44-fold higher TIAC for pig 1 was caused by additional spill-in from the surrounding tissues of the kidney in pig 1.

Based on the head-to-head comparison of the pig 1 TIAC by using both image modalities, the use of MP1S imaging resulted in considerably lower kidney TIAC. In addition, eliminating late time points from the time activity curve of pig 1 kidney caused a decrease in TIACs, up to a factor of 2.4.

As a result of missing information with eliminating late two time points, the selected fit parameters did not represent well the original biodistribution which can be observed by the corresponding increase in TIAC error values. Eliminating late time points, independent of used scan techniques, resulted in an increase for TIAC error values (up to 4.4 times).

The bone marrow is another organ-at-risk in ^{177}Lu labelled treatments. Bone marrow dosimetry can be performed by either blood based approaches or image based calculations including scans e.g. of lumbar vertebrae 2-4 (LV2-4) (*66,67*). As we have no data on neither the activity contents of bone marrow containing tissues nor LV2-4 segmented uptake values for the OPS201 mice and patients, a comparison of bone marrow dosimetry based on images could not be performed. In addition, associated with the visible spine uptake in pigs (in compare to no spine uptake in patients), image-based method was also not performed for bone marrow absorbed dose calculations. For future studies, it is beneficial to have bone marrow tissue samples and/or corresponding image data of patients including late time points (more than 100 h) for an improved comparison of image- and blood-based bone marrow TIACs calculation and, as a consequence, absorbed doses. Also, for future studies, additional investigations to analyze the difference between blood-based and image-based bone marrow dosimetry methods in an increased number of patients with gender specific analyses will improve bone marrow dosimetry.

6. Conclusion

^{68}Ga-OPS202 showed promising biodistribution and imaging properties, with optimal tumor contrast between one and two hours after injection. The result of this phase I study showed that ^{68}Ga-OPS202 is rapidly cleared from the blood, resulting in low background activity, especially in the liver and gastrointestinal tract. As a result of having lower background activity than other ^{68}Ga labelled compounds, advanced lesion detection is obtained which directly improve the diagnostic staging. Dosimetry analysis revealed that the administration of ^{68}Ga-OPS202 delivers an acceptable radiation dose to organs and there were no safety signals of concern. The effective dose delivered by ^{68}Ga-OPS202 to organs is similar to the dose delivered by other ^{68}Ga-labeled somatostatin receptor analogs.

^{177}Lu-OPS201 was well tolerated in each species and produced no abnormal physiological or behavioral signs. Based on analyses of in vivo distributions and absorbed doses of ^{177}Lu-OPS201, the radiation exposure is acceptable and comparable with the literature in pigs and humans. There was no evidence that especially patients enrolled in the ^{177}Lu-OPS201 study would be exposed to an unjustified overexposure of the radioactivity. In preclinical studies, the potential interspecies differences need to be analyzed carefully due to inconsistent spine and spleen uptake results. Extrapolation methods are required to be applied in preclinical studies in order to predict the biokinetics, TIACs, absorbed doses and dosimetry in humans accurately. If the organ mass ratios between the species are high, either time scaling or combination of relative mass and time scaling is the most adequate scaling method for TIACs, which minimize the interspecies differences. The analysis of the fit functions and the TIACs show that, pigs are better mimicking human biokinetics. Furthermore, this study including experimental 3D printed phantom experiment shows that, for the ^{177}Lu-labeled dosimetry studies, using multiple SPECT/CT images and follow-up times at late time points has a great impact on the calculation of absorbed dose values. Therefore, using multiple SPECT/CT images improves the dosimetry and more than 120 h are required for TIAC calculations to appropriately represent the area under the curve and to analyze both biokinetics and dosimetry accurately.

7. List of Abbreviations

$\tilde{A}$: The Total Cumulated Activity within an Organ

$\widetilde{\mathrm{A}}_{\mathrm{RM}}$: Time-Integrated Activity in the Red Bone Marrow

A%: The Percentage Values Corresponding To the Injected Radioactivity

A_0: The Amount of Injected Activity

A(0): The Amount Of Radioactivity in an Initial Time Point

A(t) : The Amount Of Radioactivity in a Certain Time Point

A: Alpha

β^-: Electron

β^+ : Positron

Bq: Becquerel

C_A: Anterior Counts

C_P: Posterior Counts

CT: Computed Tomography

CV: Coefficient of Variation

$\overline{D}$: Absorbed Dose

DF: Decay Factor

DOTATATE: DOTA-[Tyr3]Octreotate

DOTATOC: DOTA-[Tyr3]Octreotide

DOTANOC: DOTA-[NaI3]Octreotide

GEP-NET: Gastroenteropancreatic Neuroendocrine Tumor

MP1S: Combination of Multiple Planar Images with One SPECT/CT Image

ICRP: International Commission on Radiological Protection

KM: Fitted Curves for the Kidneys Including Fit Function Parameters from NUKFIT for Mice

KP: Fitted Curves for the Kidneys Including Fit Function Parameters from NUKFIT for Pigs

KH: Fitted Curves for the Kidneys Including Fit Function Parameters from NUKFIT for Humans

LV2-4: Lumbar Vertebra 2-4

m_{RM}: Mass of the Red Marrow

NET: Neuroendocrine Tumor

OPS201: DOTA-JR11 or Cpac[D-Cys-Aph(Hor)-D-Aph(Cbm)-Lys-Thr-Cys]-D-Tyr-NH2

OPS202: NODAGA-JR11

OSEM: Ordered Subset Expectation Maximization

PET: Positron Emission Tomography

Phantom NOBG: Phantom without Background Activity

Phantom BG: Phantom with Background Activity

PRRT: Peptide receptor radionuclide therapy

PVE: Partial Volume Effect

ROI: Region of Interests

RMBLR: Red Marrow–to–Blood Activity Concentration

S: The Radionuclide-Specific Quantity Representing the Mean Absorbed Dose Rate to Target Tissue at a Time Point after Administration per Unit Activity Present in Source Tissue

SD: Standard Error

SPECT/CT: Single-Photon Emission Computed Tomography

SSTR: Somatostatin Receptor Subtype

STD: Standard Deviation

Sv: Sievert

t: Time

T: Tissue

$T_{1/2:}$ Half-Life of a Radionuclide

TAC: Separately Fitted Time-Activity Curve

TIAC or $\widetilde{A}$: Time-Integrated Activity Coefficient Value

TP: Time Points

VOI: Volume of Interest

^{68}Zn: Zinc-68

λ: Decay Constant for a Radionuclide

γ: Gamma

^{68}Ga: Gallium-68

^{68}Ge: Germanium-68

^{64}Ni: Nickel-64

^{177}Lu: Lutetium-177

W_R: The Radiation Weighting Factor

W_T: The Tissue Weighting Factor

WB: Whole Body

$\bar{\nu}e$: Antineutrino

νe: Neutrino

8. References

1. Cescato R, Waser B, Fani M, Reubi JC. Evaluation of ^{177}Lu-DOTA-sst2 antagonist versus ^{177}Lu-DOTA-sst2 agonist binding in human cancers in vitro. *J Nucl Med.* 2011;52:1886-1890.

2. Beykan S, Dam JS, Eberlein U, et al. ^{177}Lu-OPS201 targeting somatostatin receptors: in vivo biodistribution and dosimetry in a pig model. *EJNMMI Res.* 2016;6:50.

3. Nicolas GP, Mansi R, McDougall L, et al. Biodistribution, Pharmacokinetics, and Dosimetry of ^{177}Lu-, ^{90}Y-, and ^{111}In-Labeled Somatostatin Receptor Antagonist OPS201 in Comparison to the Agonist ^{177}Lu-DOTATATE: The Mass Effect. *J Nucl Med.* 2017;58:1435-1441.

4. Wild D, Fani M, Fischer R, et al. Comparison of somatostatin receptor agonist and antagonist for peptide receptor radionuclide therapy: a pilot study. *J Nucl Med.* 2014;55:1248-1252.

5. Wild D, Fani M, Behe M, et al. First clinical evidence that imaging with somatostatin receptor antagonists is feasible. *J Nucl Med.* 2011;52:1412-1417.

6. Beykan S, Fani M, Jensen SB, et al. In Vivo Biokinetics of ^{177}Lu-OPS201 in Mice and Pigs as a Model for Predicting Human Dosimetry. *Contrast Media Mol Imaging.* 2019;2019:6438196.

7. Fani M, Nicolas GP, Wild D. Somatostatin Receptor Antagonists for Imaging and Therapy. *J Nucl Med.* 2017;58:61S-66S.

8. Hennrich U, Kopka K. Lutathera((R)): The First FDA- and EMA-Approved Radiopharmaceutical for Peptide Receptor Radionuclide Therapy. *Pharmaceuticals (Basel).* 2019;12.

9. Dalm SU, Nonnekens J, Doeswijk GN, et al. Comparison of the therapeutic response to treatment with a 177-lutetium labeled somatostatin receptor agonist and antagonist in preclinical models. *J Nucl Med.* 2015.

10. Van Essen M, Krenning EP, Kam BL, de Jong M, Valkema R, Kwekkeboom DJ. Peptide-receptor radionuclide therapy for endocrine tumors. *Nat Rev Endocrinol.* 2009;5:382-393.

11. Ginj M, Zhang H, Waser B, et al. Radiolabeled somatostatin receptor antagonists are preferable to agonists for in vivo peptide receptor targeting of tumors. *Proc Natl Acad Sci U S A.* 2006;103:16436-16441.

12. Kupitz D, Wetz C, Wissel H, et al. Software-assisted dosimetry in peptide receptor radionuclide therapy with 177Lutetium-DOTATATE for various imaging scenarios. *PLoS One.* 2017;12:e0187570.

13. Sparks RB AB. Comparison of the Effectiveness of Some Common Animal Data Scaling Techniques in Estimating Human Radiation Dose. *Sixth International Radiopharmaceutical Dosimetry Symposium.* 1999:705-716.

14. Lindstedt SL, Schaeffer PJ. Use of allometry in predicting anatomical and physiological parameters of mammals. *Lab Anim.* 2002;36:1-19.

15. Nicolas GP, Beykan S, Bouterfa H, et al. Safety, Biodistribution, and Radiation Dosimetry of (68)Ga-OPS202 in Patients with Gastroenteropancreatic Neuroendocrine Tumors: A Prospective Phase I Imaging Study. *J Nucl Med.* 2018;59:909-914.

16. Nicolas GP, Schreiter N, Kaul F, et al. Sensitivity Comparison of ^{68}Ga-OPS202 and ^{68}Ga-DOTATOC PET/CT in Patients with Gastroenteropancreatic Neuroendocrine Tumors: A Prospective Phase II Imaging Study. *J Nucl Med.* 2018;59:915-921.

17. Krebs S, Pandit-Taskar N, Reidy D, et al. Biodistribution and radiation dose estimates for ^{68}Ga-DOTA-JR11 in patients with metastatic neuroendocrine tumors. *Eur J Nucl Med Mol Imaging.* 2019;46:677-685.

18. Kletting P, Schimmel S, Hänscheid H, et al. The NUKDOS software for treatment planning in molecular radiotherapy. *Z Med Phys.* 2015;25:264-274.

19. Podgorsak EB. *Radiation oncology physics : a handbook for teachers and students / editor*. VIENNA: International Atomic Energy Agency; 2005.

20. Powsner RAPaER. *Essential Nuclear Medicine Physics- 2nd Edition*. USA, UK, Australia: Blackwell Publishing Ltd; 2006.

21. Simon Cherry JS, Michael Phelps. *Physics in Nuclear Medicine*. 4th Edition ed; 2012.

22. *Quantitative Nuclear Medicine Imaging: Concepts, Requirements and Methods*. Vienna: INTERNATIONAL ATOMIC ENERGY AGENCY; 2014.

23. Hofland LJ, Lamberts SW. The pathophysiological consequences of somatostatin receptor internalization and resistance. *Endocr Rev.* 2003;24:28-47.

24. Velikyan I. Prospective of ^{68}Ga-radiopharmaceutical development. *Theranostics.* 2013;4:47-80.

25. Velikyan I. Positron emitting ^{68}Ga-based imaging agents: chemistry and diversity. *Med Chem.* 2011;7:345-379.

26. Velikyan I. ^{68}Ga-Based radiopharmaceuticals: production and application relationship. *Molecules.* 2015;20:12913-12943.

27. Lassmann M, Eberlein U. Radiation Dosimetry Aspects of ^{177}Lu. *Curr Radiopharm.* 2015;8:139-144.

28. Bodei L, Mueller-Brand J, Baum RP, et al. The joint IAEA, EANM, and SNMMI practical guidance on peptide receptor radionuclide therapy (PRRNT) in neuroendocrine tumours. *Eur J Nucl Med Mol Imaging.* 2013;40:800-816.

29. Malcolm J, Falzone N, Lee BQ, Vallis KA. Targeted Radionuclide Therapy: New Advances for Improvement of Patient Management and Response. *Cancers (Basel).* 2019;11.

30. Garske-Roman U, Sändstrom M, Fross Baron K, et al. Prospective observational study of ^{177}Lu-DOTA-octreotate therapy in 200 patients with advanced metastasized neuroendocrine tumours (NETs): feasibility and impact of a dosimetry-guided study protocol on outcome and toxicity. *Eur J Nucl Med Mol Imaging.* 2018;45:970-988.

31. Siegel JA, Thomas SR, Stubbs JB, et al. MIRD pamphlet no. 16: Techniques for quantitative radiopharmaceutical biodistribution data acquisition and analysis for use in human radiation dose estimates. *J Nucl Med.* 1999;40:37S-61S.

32. Bolch WE, Eckerman KF, Sgouros G, Thomas SR. MIRD pamphlet No. 21: a generalized schema for radiopharmaceutical dosimetry--standardization of nomenclature. *J Nucl Med.* 2009;50:477-484.

33. Li T, Ao ECI, Lambert B, Brans B, Vandenberghe S, Mok GSP. Quantitative Imaging for Targeted Radionuclide Therapy Dosimetry - Technical Review. *Theranostics.* 2017;7:4551-4565.

34. Tran-Gia J, Lassmann M. Characterization of Noise and Resolution for Quantitative ^{177}Lu SPECT/CT with xSPECT Quant. *J Nucl Med.* 2019;60:50-59.

35. Ljungberg M, Celler A, Konijnenberg MW, et al. MIRD Pamphlet No. 26: Joint EANM/MIRD Guidelines for Quantitative ^{177}Lu SPECT Applied for Dosimetry of Radiopharmaceutical Therapy. *J Nucl Med.* 2016;57:151-162.

36. Siegel JA, Wu RK, Maurer AH. The buildup factor: effect of scatter on absolute volume determination. *J Nucl Med.* 1985;26:390-394.

37. Ljungberg M, Sjogreen Gleisner K. Personalized Dosimetry for Radionuclide Therapy Using Molecular Imaging Tools. *Biomedicines.* 2016;4.

38. Rinscheid A, Lee J, Kletting P, Beer AJ, Glatting G. A simulation-based method to determine optimal sampling schedules for dosimetry in radioligand therapy. *Z Med Phys.* 2019;29:314-325.

39. Kletting P, Schimmel S, Kestler HA, et al. Molecular radiotherapy: the NUKFIT software for calculating the time-integrated activity coefficient. *Med Phys.* 2013;40:102504.

40. Salek N, Mehrabi M, Shirvani Arani S, et al. Production, quality control, and determination of human absorbed dose of no carrier added ^{177}Lu-risedronate for bone pain palliation therapy. *J Labelled Comp Radiopharm.* 2017;60:20-29.

41. Stabin MG, Sparks RB, Crowe E. OLINDA/EXM: the second-generation personal computer software for internal dose assessment in nuclear medicine. *J Nucl Med.* 2005;46:1023-1027.

42. Tse J, Geoghegan S. Calculations of dose point kernels of ^{64}Cu in different media with PENELOPE Monte Carlo code. *Med Phys.* 2019;46:2422-2429.

43. Grimes J, Celler A. Comparison of internal dose estimates obtained using organ-level, voxel S value, and Monte Carlo techniques. *Med Phys.* 2014;41:092501.

44. 1990 Recommendations of the International Commission on Radiological Protection. *Ann ICRP.* 1991;21:1-201.

45. The 2007 Recommendations of the International Commission on Radiological Protection. ICRP publication 103. *Ann ICRP.* 2007;37:1-332.

46. Mountford PJ, Temperton DH. Recommendations of the International Commission on Radiological Protection (ICRP) 1990. *Eur J Nucl Med.* 1992;19:77-79.

47. Bolch WE, Eckerman KF, Sgouros G, Thomas SR. MIRD pamphlet No. 21: a generalized schema for radiopharmaceutical dosimetry-standardization of nomenclature. *J Nucl Med.* 2009;50:477-484.

48. Fisher DR, Fahey FH. Appropriate Use of Effective Dose in Radiation Protection and Risk Assessment. *Health Phys.* 2017;113:102-109.

49. Basic anatomical and physiological data for use in radiological protection: reference values. A report of age- and gender-related differences in the anatomical and physiological characteristics of reference individuals. ICRP Publication 89. *Ann ICRP.* 2002;32:5-265.

50. Hagmarker L, Svensson J, Ryden T, et al. Bone marrow absorbed doses and correlations with hematological response during ^{177}Lu-DOTATATE treatments are influenced by image-based dosimetry method and presence of skeletal metastases. *J Nucl Med.* 2019.

51. Shen S, Meredith RF, Duan J, et al. Improved prediction of myelotoxicity using a patient-specific imaging dose estimate for non-marrow-targeting ^{90}Y-antibody therapy. *J Nucl Med.* 2002;43:1245-1253.

52. Herrmann K, Lapa C, Wester HJ, et al. Biodistribution and radiation dosimetry for the chemokine receptor CXCR4-targeting probe ^{68}Ga-pentixafor. *J Nucl Med.* 2015;56:410-416.

53. Forrer F, Krenning EP, Kooij PP, et al. Bone marrow dosimetry in peptide receptor radionuclide therapy with [177Lu-DOTA(0),Tyr(3)]octreotate. *Eur J Nucl Med Mol Imaging.* 2009;36:1138-1146.

54. Ferrer L, Kraeber-Bodere F, Bodet-Milin C, et al. Three methods assessing red marrow dosimetry in lymphoma patients treated with radioimmunotherapy. *Cancer.* 2010;116:1093-1100.

55. Andersson M, Johansson L, Eckerman K, Mattsson S. IDAC-Dose 2.1, an internal dosimetry program for diagnostic nuclear medicine based on the ICRP adult reference voxel phantoms. *EJNMMI Res.* 2017;7:88.

56. Hartmann H, Zophel K, Freudenberg R, et al. [Radiation exposure of patients during ^{68}Ga-DOTATOC PET/CT examinations]. *Nuklearmedizin.* 2009;48:201-207.

57. Sandstrom M, Velikyan I, Garske-Roman U, et al. Comparative biodistribution and radiation dosimetry of ^{68}Ga-DOTATOC and ^{68}Ga-DOTATATE in patients with neuroendocrine tumors. *J Nucl Med.* 2013;54:1755-1759.

58. ICRP. Radiation dose to patients from radiopharmaceuticals. Addendum 3 to ICRP Publication 53. ICRP Publication 106. Approved by the Commission in October 2007. *Ann ICRP.* 2008;38:1-197.

59. Walker RC, Smith GT, Liu E, Moore B, Clanton J, Stabin M. Measured human dosimetry of ^{68}Ga-DOTATATE. *J Nucl Med.* 2013;54:855-860.

60. Lassmann M, Hanscheid H, Reiners C, Thomas SR. Blood and bone marrow dosimetry in radioiodine therapy of differentiated thyroid cancer after stimulation with rhTSH. *J Nucl Med.* 2005;46:900-901; author reply 901.

61. Pettinato C, Sarnelli A, Di Donna M, et al. ^{68}Ga-DOTANOC: biodistribution and dosimetry in patients affected by neuroendocrine tumors. *Eur J Nucl Med Mol Imaging.* 2008;35:72-79.

62. Eberlein U, Nowak C, Bluemel C, et al. DNA damage in blood lymphocytes in patients after ^{177}Lu peptide receptor radionuclide therapy. *Eur J Nucl Med Mol Imaging.* 2015;42:1739-1749.

63. Sandstrom M, Garske-Roman U, Granberg D, et al. Individualized dosimetry of kidney and bone marrow in patients undergoing ^{177}Lu-DOTA-octreotate treatment. *J Nucl Med.* 2013;54:33-41.

64. Nicolas G BR, Herrmann K, Lassmann M, et al. Phase 1/2 open-label trial to assess the safety and preliminary efficacy of ^{177}Lu-OPS201 as peptide receptor radionuclide therapy in patients with somatostatin receptor-positive, progressive neuroendocrine tumours. Presented at Society for Endocrinology BES 2017, Harrogate, UK Endocrine Abstracts 50 PL1; 2017.

65. De Jong M, Maina T. Of mice and humans: are they the same?--Implications in cancer translational research. *J Nucl Med.* 2010;51:501-504.

66. Blakkisrud J, Londalen A, Dahle J, et al. Red Marrow-Absorbed Dose for Non-Hodgkin Lymphoma Patients Treated with ^{177}Lu-Lilotomab Satetraxetan, a Novel Anti-CD37 Antibody-Radionuclide Conjugate. *J Nucl Med.* 2017;58:55-61.

67. Hindorf C, Glatting G, Chiesa C, Linden O, Flux G, Committee ED. EANM Dosimetry Committee guidelines for bone marrow and whole-body dosimetry. *Eur J Nucl Med Mol Imaging.* 2010;37:1238-1250.

68. M.M.Be VC, C.Dulieu, E.Browne, V.Chechev, N.Kuzmenko, R.Helmer, A.Nichols, E.Schonfeld, R.Dersch. Monographie BIPM-5 - Table of Radionuclides,. *Bureau International des Poids et Mesures.* 2004;2:151-242.

iii. Appendix

Table 9.1: Time-Integrated Activity Coefficients (TIAC (unit: h)) for the Selected Organs of the OPS202 Injected Patients

	P1 TIAC (h)	P2 TIAC (h)	P3 TIAC (h)	P4 TIAC (h)	P5 TIAC (h)	P6 TIAC (h)	P7 TIAC (h)	P8 TIAC (h)	P9 TIAC (h)	P10 TIAC (h)	P11 TIAC (h)	P12 TIAC (h)
WB	1.377	1.327	1.211	1.405	1.406	1.335	1.420	1.391	1.321	1.375	1.273	1.208
RB	0.947	1.010	0.762	1.007	1.021	0.974	0.977	1.073	0.902	1.006	0.898	0.748
Liver	0.071	0.031	0.078	0.070	0.084	0.045	0.095	0.063	0.078	0.104	0.070	0.077
Kidneys	0.070	0.043	0.055	0.062	0.065	0.079	0.052	0.031	0.054	0.046	0.051	0.077
Heart	0.013	0.010	0.017	0.009	0.009	0.010	0.020	0.014	0.012	0.007	0.010	0.009
Adrenal glands	0.001	0.000	0.001	0.001	0.001	0.001	0.001	0.001	0.001	0.001	0.002	0.001
Gallblad.	NA	NA	NA	NA	0.001	NA	0.001	NA	NA	0.001	0.001	NA
LLI	0.019	0.015	0.016	0.018	0.021	0.021	0.022	0.018	0.013	0.012	0.019	0.020
ULI	0.019	0.015	0.016	0.018	0.021	0.021	0.022	0.018	0.013	0.012	0.019	0.020
SI	0.019	0.015	0.016	0.018	0.021	0.021	0.022	0.018	0.013	0.012	0.019	0.020
Stomach	0.019	NA	0.016	0.018	0.021	0.021	0.022	0.018	0.013	0.012	0.019	0.020
Lung	0.051	0.045	0.052	0.048	0.030	0.041	0.064	0.047	0.045	0.025	0.042	0.038
Pancreas	0.003	0.002	0.001	0.004	0.003	NA	0.002	0.002	0.003	0.002	0.004	0.001
Spleen	0.018	0.012	0.001	0.030	0.013	NA	0.050	0.013	0.048	0.035	0.022	0.050
LV2-4	0.002	0.002	0.002	0.002	0.001	0.002	0.002	0.001	0.003	0.001	NA	0.002
Blood*	0.045	0.053	0.078	0.059	0.040	0.032	0.038	0.043	0.032	0.026	0.003	0.032
RedBM	0.025	0.030	0.024	0.032	0.019	0.037	0.029	0.022	0.047	0.012	NA	0.024
Uri.blad.	0.101	0.100	0.155	0.070	0.076	0.065	0.042	0.052	0.081	0.087	0.098	0.104

Patients were numbered from asP1-P2. Where, WB: whole body, RB: remainder, Gallblad.: gallbladder, LLI: lower large intestine, ULI: upper large intestine, SI: small intestine, LV2-4: lumbar vertebra 2-4, RedBM: red bone marrow, Uri.blad: urinary bladder. NA: not available.

*The Unit of blood is h/L.

Table 9.2: Calculated lambda values used to create the TACs by using the optimal fit function parameters from NUKFIT (*39*) for each species' organs and blood including standard error (SD) and coefficient of variation (CV) values determined assuming Gaussian error propagation

Blood:

Mice Blood

	Value	SD	CV	NUKFIT function used
A1	0.416	0.0596	0.1432	$\mathrm{A1} \cdot \mathrm{e}^{-(\lambda_1+\lambda_{\mathrm{phys}})\cdot t} + \mathrm{A2} \cdot \mathrm{e}^{-(\lambda_{\mathrm{phys}})\cdot t}$
λ_1	0.3794	0.0509	0.1342	
A2	0.0107	7.6E-04	0.0710	

Pig Blood

	Value	SD	CV	NUKFIT function used
A1	0.0208	8.2E-04	0.0395	$\mathrm{A1} \cdot \mathrm{e}^{-(\lambda_1+\lambda_{\mathrm{phys}})\cdot t} + \mathrm{A2} \cdot \mathrm{e}^{-(\lambda_2+\lambda_{\mathrm{phys}})\cdot t} + \mathrm{A3} \cdot \mathrm{e}^{-(\lambda_3+\lambda_{\mathrm{phys}})\cdot t}$
λ_1	11.8943	0.5747	0.0483	
A2	0.0020	8.3E-05	0.0412	
λ_2	0.4066	0.0195	0.0480	
A3	1.7E-04	8.6E-06	0.0511	
λ_3	0.0076	3.1E-04	0.0405	

Human Blood

	Value	SD	CV	NUKFIT function used
A1	0.0022	4.1E-04	0.1848	$\mathrm{A1} \cdot \mathrm{e}^{-(\lambda_1+\lambda_{\mathrm{phys}})\cdot t} + \mathrm{A2} \cdot \mathrm{e}^{-(\lambda_2+\lambda_{\mathrm{phys}})\cdot t}$
λ_1	1.4713	0.3513	0.2388	
A2	6.2E-04	6.6E-05	0.1066	
λ_2	0.0609	0.0072	0.1181	

For ^{177}Lu: $\lambda_{\mathrm{phys}} = \frac{\ln(2)}{\mathrm{T}_{1/2}} = \frac{0.6931}{159.93\ \mathrm{h}} = 0.00435\ \mathrm{h}$ (*68*).

Liver:

Mice Liver

	Value	SD	CV	NUKFIT function used
A1	1.0394	0.2313	0.2225	$\mathrm{A1} \cdot \mathrm{e}^{-(\lambda_1+\lambda_{\mathrm{phys}})\cdot t} + \mathrm{A2} \cdot \mathrm{e}^{-(\lambda_{\mathrm{phys}})\cdot t}$
λ_1	0.4724	0.1160	0.2455	
A2	0.3168	0.0183	0.0577	

Pig Liver

	Value	SD	CV	NUKFIT function used
A1	2.9475	0.4470	0.1517	$\mathrm{A1} \cdot \mathrm{e}^{-(\lambda_1+\lambda_{\mathrm{phys}})\cdot t} + \mathrm{A2} \cdot \mathrm{e}^{-(\lambda_2+\lambda_{\mathrm{phys}})\cdot t}$
λ_1	0.138	0.0669	0.4839	
A2	3.7373	0.1986	0.0531	
λ_2	0.0053	3.3E-04	0.0620	

Human Liver

	Value	SD	CV	NUKFIT function used
A1	5.4340	0.3613	0.0665	$\mathrm{A1} \cdot \mathrm{e}^{-(\lambda_1+\lambda_{\mathrm{phys}})\cdot t}$
λ_1	0.0059	0.0018	0.3005	

Kidney:

Mice Kidneys

	Value	SD	CV	NUKFIT function used
A1	2.3300	0.1580	0.0678	$\mathrm{A1} \cdot \mathrm{e}^{-(\lambda_1+\lambda_{\mathrm{phys}})\cdot t} + \mathrm{A2} \cdot \mathrm{e}^{-(\lambda_{\mathrm{phys}})\cdot t}$
λ_1	0.0183	0.0031	0.1683	
A2	0.1790	0.0679	0.3794	

Pig Kidneys

	Value	SD	CV	NUKFIT function used
A1	6.0940	0.1999	0.0328	$\mathrm{A1} \cdot \mathrm{e}^{-(\lambda_1+\lambda_{\mathrm{phys}})\cdot t} - \mathrm{A1} \cdot \mathrm{e}^{-(\lambda_2+\lambda_{\mathrm{phys}})\cdot t}$
λ_1	0.0036	2.43E-04	0.0682	
λ_2	1.7558	0.1996	0.1137	

Human Kidneys

	Value	SD	CV	NUKFIT function used
A1	4.7877	0.3183	0.0665	$\mathrm{A1} \cdot \mathrm{e}^{-(\lambda_1+\lambda_{\mathrm{phys}})\cdot t}$
λ_1	0.0038	0.0018	0.4588	

Table 9.3.a: The median and mean percentage injected radioactivity (A%) values per ml in blood of mice and humans with corresponding standard deviation (STD)

Time(h)	Median % A/ml Blood Mice	Mean A% /ml Blood Mice	STD
1	0.296	0.1305	0.030
4	0.099	0.0332	0.013
24	0.025	0.0085	0.005
72	0.007	0.0036	0.003
Time(h)	Median % A/ml Blood Humans	Mean A% /ml Blood Humans	STD
0.3	0.0020	0.0028	0.003
0.5	0.0016	0.0022	0.002
1	0.0010	0.0016	0.002
2	0.0007	0.0011	0.001
3	0.0006	0.0009	0.001
5	0.0004	0.0007	0.001
23	0.0001	0.0002	0.000

Table 9.3.b: The mean percentage injected radioactivity (A%) values per ml in kidneys and liver of mice and humans with corresponding standard deviation (STD)

Time(h)	Mean A% Kidneys Mice	STD
1	2.600	0.162
4	2.100	0.135
24	1.570	0.127
72	0.590	0.042
168	0.140	0.131

Time(h)	Mean A% Kidneys Humans	STD
1	5.585	2.140
3	5.303	1.713
24	4.128	1.427
72	2.678	1.072

Time(h)	Mean A% Liver Mice	STD
1	0.970	0.308
4	0.470	0.132
24	0.236	0.052
72	0.170	0.042
168	0.196	0.042

Time(h)	Mean A% Liver Humans	STD
1	4.978	2.548
3	4.480	2.289
24	4.015	1.825
72	2.688	1.148

iv. List of Tables

Table 2.6.1: Somatostatin Analogue Affinity Table

Table 2.7.1: Selected Radionuclides Used in Clinical PET, SPECT and Radiotherapy, Their Production Mode and Decay Properties

Table 2.10.1: The Tissue Weighting Factors (WT) in ICRP 60 and in ICRP 103 Publications

Table 3.1: Information about Species for OPS201 and OPS202 Labelled Preclinical and Clinical Studies

Table 3.3: Selected Organs for the In-Vivo Biodistribution Analysis of ^{177}Lu-OPS201

Table 4.1.1: Calculated Mean absorbed Dose Values and Effective Dose Coefficient Values for Each Species

Table 4.1.2: Effective Dose Values for ^{68}Ga Labelled Compounds

Table 4.2.2: Time-Integrated Activity Coefficients (TIAC (unit: h)) for the Selected Organs of the Animals Based On The Different Scaling Methods To Estimate Human TIAC Using Either Mice Or Pig Data Set As A Reference

Table 4.2.1: Time-Integrated Activity Coefficients (TIAC (unit: h)) of the Selected Organs for each species with Respective Error Values Calculated by NUKFIT with An Assumption of 10% Systematic Error

Table 4.3: The Calculated TIACs by Using Multiple SPECT/CT and MP1S Imaging for the Phantom and Pig 1 Based on Using Different Sets of Time Points

Table 9.1: Time-Integrated Activity Coefficients (TIAC (unit: h)) for the Selected Organs of the OPS202 Injected Patients with corresponding standard deviation (STD)

Table 9.2: Calculated Lambda Values Used to Create the TACs by Using the Optimal Fit Function Parameters From NUKFIT for Each Species' Organs and Blood Including Standard Error (SD) and Coefficient of Variation (CV) Values Determined Assuming Gaussian Error Propagation

Table 9.3.a: The Median and Mean Percentage Injected Radioactivity (A%) Values per Ml in Blood of Mice and Humans with Corresponding Standard Deviation (STD)

Table 9.2.3: The Mean Percentage Injected Radioactivity (A%) Values per Ml in Kidneys and Liver of Mice and Humans with Corresponding Standard Deviation (SD)

v. List of Figures

Figure 2.5.2: The Steps in Iterative Reconstruction

Figure 2.6.1: Mechanism Difference between Agonistic and Antagonistic Peptides

Figure 2.8.1: Schematic Overview of Targeted Peptide Receptor Radionuclide

Figure 2.10.6: Anterior and Posterior Views of Planar Image of a Pig Including ROIs

Figure 2.10.7: Axial, Sagittal and Coronal views of a SPECT/CT for ^{177}Lu injected Pig 1

Figure3.8.1: Dimensions of Ellipsoid, Axial, Coronal and Sagittal views of Pig 1 CT

Figure 3.8.2: The NEMA NU2-2001 PET/SPECT-Phantom Including 3D Printed Kidney Phantom

Figure 4.1: Percentage Activity (A%) of the Kidney versus Time for OPS202 Injected Patients

Figure 4.2.1: Time Activity Curves of the Kidneys Based on VOI and Well-Type Gamma Counter Analysis for Each Species

Figure 4.2.2: Time Activity Curves of the Liver Based on VOI and Well-Type Gamma Counter Analysis for Each Species

Figure 4.2.3: Time Activity Curves of Blood Based on VOI and Well-Type Gamma Counter Analysis for Each Species

Figure 4.3.1: Time Activity Curves for the Kidney Phantom with/without Background Activity and Pig 1 Based on Multiple SPECT/CT and MP1S Imaging

Figure 4.3.2: The Difference on Kidney TIACs with corresponding NUKDOS error values, in the Phantom with/without Background Activity and Pig 1 Calculated by Using NUKDOS with Eliminating the either the last or the last two Time Points

vi. Affidavit / Eidesstattliche Erklärung

Affidativ

I hereby confirm that my thesis entitled Implementation and Optimization of Dosimetry for Theranostics in Radiopeptide Therapies is the result of my own work. I did not receive any help or support from commercial consultants. All sources and / or materials applied are listed and specified in the thesis.

Furthermore, I confirm that this thesis has not yet been submitted as part of another examination process neither in identical nor in similar form.

Place, Date Signature

Eidesstattliche Erklärung

Hiermit erkläre ich an Eides statt, die Dissertation Implementation and Optimization of Dosimetry for Theranostics in Radiopeptide Therapies eigenständig, d.h. insbesondere selbständig und ohne Hilfe eines kommerziellen Promotionsberaters, angefertigt und keine anderen als die von mir angegebenen Quellen und Hilfsmittel verwendet zu haben.

Ich erkläre außerdem, dass die Dissertation weder in gleicher noch in ähnlicher Form bereits in einem anderen Prüfungsverfahren vorgelegen hat.

Ort, Datum Unterschrift

vii. Acknowledgments

I would like to acknowledge my great supervisor Prof. Dr. Michael Lassmann for giving me the opportunity to work on this topic and his continuous teaching support offered during my PhD time period and for sure his advices, moral supports giving me the strength to carry on along the time period and learning process.

The majority of the raw data for this thesis could not have been used without the generosity of Prof. Dr. Damian Wild, Dr. Guillaume Nicolas and Prof. Dr. Melpomeni Fani (University Hospital of Basel), by sharing their data. Also I gratefully acknowledge the support of Dr. Jens Kaufmann (OctreoPharm Sciences GmbH) and Dr. Svend Borup Jensen (University Hospital of Aalborg).

This work would not have been also possible without the help, guidance and assistance of Ms. Susanne Schlögl and Dr. Johannes Tran-Gia. Thank you for all the help for my experiments, all the time spent dealing with the cameras, the good jokes and laughs, and for being not just a colleague but also a good friend. In addition I would like to thank Hashan Neumayer for his valuable effort and contribution to the 3D printing. I would also like to express my gratitude to the members of my PhD committee Prof. Dr. Gerhard Glatting and Prof. Dr. med. Andreas K. Buck. Thank you for all the feedback and discussions. I am also grateful for the valuable feedback and corrections of Dr. Uta Eberlein on my thesis.

In addition, I would like to thank my family due to their moral supports and motivations. Mom and Dad, this has finally become a reality, I am about to become the first doctor in the family. Thank you so much for all the love you have given me throughout my whole life and for all the sacrifices you have done for me. Thank you for all the great moments we have had as a beautiful family. Mom I could not have done this without her endless support that gives me strength to overcome all the difficulties that I had. Special thanks to Prof. Dr. Ş. İpek Karaaslan, Assoc. Prof. Dr. Nalan A. Selçuk and Dr. Türkay Toklu who prepared my background so that I ended up in Germany. I also greatly appreciate to have Gülayse Gürsoy Sayed, Sameh Sayed and Jessica Soares Machado who are always near my site, taking care of me and trying their best to motivate me all the time. Additionally, I would like to thank to my dear team members Maikol Salas Ramirez for all his effort in salsa lectures and his moral support and sure Sarah Schumann for her 90s party invitations and trying to increase my music background. I have to admit that dancing in the salsa and 90s parties was kind of motivation sessions. Finally I really want to thank the all members and staff of the Nuclear Medicine Department at Würzburg Universitätsklinikum.

The thesis is dedicated:

To my mom Atiye Ulutekin Beykan who taught me always moving on despite to all type of difficulties and always supports me in any conditions,

To my grandmother Seval Ulutekin who is the reason of my great and happy childhood with which I became a positive person,

To my aunts Narin Ulutekin Araz and Mediha Ulutekin Zaman who taught me alphabet and writing (basically helped me for my first step in my education life) and taught me to be always a respectful and responsible person.

Bu doktora tezi hayatta her zaman her koşulda bana destek olan ve bana karşılaşacağım zorluklara rağmen asla vazgeçmemeyi öğreten anneme, mutlu bir çocukluk geçirmemin nedeni olan ve bu yüzden hayata hep olumlu bakmamı sağlayan anneanneme, bana okuma yazma öğretip eğitim hayatımın ilk adımlarını attıran Narin teyzeme, bana terbiyeyi ve güzel konuşmayı öğretip her daim saygılı bir birey olmamı sağlayan Mediha teyzeme ithaf edilmiştir.

Seval Beykan

viii. Curriculum Vitae

SEVAL BEYKAN